A Search for Squarks and Gluinos in $p\bar{p}$ Collisions at $\sqrt{s} = 1.8$ TeV with the DØ Detector

A Dissertation Presented

by

Marc Francis Paterno

to

The Graduate School

in Partial Fulfillment of the Requirements

for the Degree of

Doctor of Philosophy

in

Physics

State University of New York
at
Stony Brook

May 1994

State University of New York
at Stony Brook

The Graduate School

Marc Francis Paterno

We, the dissertation committee for the above candidate for the Doctor of Philosophy degree, hereby recommend acceptance of the dissertation.

Advisor
Professor Chang Kee Jung
Department of Physics

Professor Robert McCarthy
Department of Physics

Professor Roderich Engelmann
Department of Physics

Professor Howard Baer
Department of Physics
Florida State University

This dissertation is accepted by the Graduate School.

Graduate School

Abstract of the Dissertation

A Search for Squarks and Gluinos in $p\bar{p}$ Collisions at $\sqrt{s} = 1.8$ TeV with the DØ Detector

by

Marc Francis Paterno

Doctor of Philosophy

in

Physics

State University of New York at Stony Brook

1994

We have searched for evidence for the production and decay of the squarks and gluinos of the Minimal Supersymmetric Standard Model (MSSM) in $p\bar{p}$ collisions at a center of mass energy of 1.8 TeV using the DØ detector at the Fermi National Accelerator Laboratory. Data corresponding to an integrated luminosity of 7.4 ± 1.0 pb^{-1} were examined for events containing large missing transverse energy ($\not{E}_T$) and three or more jets in the absence of prompt leptons. We observed no excess above the expected yield from Standard Model processes. For the choice of MSSM parameters $\tan\beta = 2$ and $\mu = -250$ GeV we set a lower limit on the mass of the gluino (for all squark masses) of 157 GeV

at the 95% confidence level. With the constraint of equal squark and gluino masses we set a lower limit of 218 GeV at the 95% confidence level. We also set a lower limit on the squark mass that varies with the mass of the gluino.

I dedicate this work to the memory of my parents, Frank and Marie, who inspired me to begin it;

to my wife, Laura, who saw me through it;

and to my children, Robert and Maria, with whom I was blessed during the process.

I love you all.

Contents

List of Figures . . . . . **xii**

List of Tables . . . . . **xiv**

Acknowledgements . . . . . **xv**

1 Introduction **1**

1.1 Symmetry 1

1.1.1 Symmetries in Physics 1

1.1.2 Symmetries of the Standard Model 2

1.1.3 A New Type of Symmetry 5

1.2 The Minimal Supersymmetric Standard Model 7

1.2.1 Why This Model? 7

1.2.2 Gauge and Higgs Field Content 8

1.2.3 Matter Field Content 10

1.2.4 Parameters of the MSSM 12

1.2.5 R-Parity Conservation 13

1.2.6 Determining the Mass Spectrum 14

1.3 Squarks and Gluinos in the MSSM 14

1.3.1 Production of Squarks and Gluinos in $p\bar{p}$ Collisions . . 14

1.3.2 Decay Modes of Squarks and Gluinos 15

1.3.3 Signatures of Squark and Gluino Decay 16

1.4 Why Do this Search? 16

2 The Apparatus 18

2.1 The Tevatron 18

2.2 The DØ Detector 20

2.2.1 The DØ Coordinate System 22

2.2.2 Central Tracking 22

2.2.3 Calorimeters 28

2.2.4 Muon Detector 35

2.2.5 Trigger 38

3 Data Collection and Processing 42

3.1 Squark and Gluino Event Signature 42

3.2 Triggering 43

3.3 Data Processing 45

3.3.1 Event Reconstruction 45

3.3.2 Filtering 46

4 Jet and $\not\!\!E_T$ Reconstruction and Corrections 49

4.1 Reconstruction 49

4.1.1 Jet Reconstruction 49

4.1.2 $\not\!\!E_T$ Reconstruction 53

4.2 Corrections 54

4.2.1 Jet Corrections 54

4.2.2 $\not\!\!E_T$ Corrections 60

5 Analysis 64

5.1 Signal Selection Cuts 64

5.1.1 Single Interaction Cut 65

5.1.2 Vertex z Cut 70

5.1.3 $\not\!\!E_T$ Cut 70

5.1.4 Three Jet Cut 71

5.1.5 ICR Cut 74

5.1.6 Jet – $\not\!\!E_T$ Correlation Cut 77

5.1.7 Electron and Muon Cuts 79

5.1.8 Noise Cut 82

5.1.9 Scanning 82

5.2 Backgrounds 84

5.2.1 Vector Boson Associated Background 86

5.2.2 QCD Associated Background 92

6 Results and Conclusion 98

6.1 Specification of the Model 98

6.2 Signal Efficiencies 100

6.3 Cross Section Limits 102

6.4 Mass Limits 105

6.5 Comparison with Previous Results 108

6.6 Future Considerations 109

List of Figures

2.1 A schematic layout of the Tevatron and its associated accelerators. 19

2.2 An isometric cutaway view of the DØ detector. 21

2.3 A side view of the DØ Central Tracking detectors. 24

2.4 An isometric view of one DØ Central Drift Chamber module. . 26

2.5 An exploded isometric view of one DØ Forward Drift Chamber. 27

2.6 An isometric view of the DØ calorimeters 29

2.7 A side view of one quarter of the DØ calorimeters and central tracking detectors. 30

2.8 A side view of the DØ detector showing the full muon system. 36

2.9 The thickness of the DØ detector 37

2.10 A schematic diagram of the DØ data acquisition and trigger system. 39

4.1 The EM fraction dependence of the jet energy correction. . . . 61

4.2 The η dependence of the jet energy correction. 61

4.3 The E_T dependence of the jet energy correction for central jets. 61

4.4 The E_T dependence of the jet energy correction for forward jets. 61

4.5 The fractional jet E_T resolution as a function of E_T for different rapidity regions. 62

5.1 Efficiency of the MITOOL. 68

5.2 The $\not{E}_T$ distribution of the 107 events passing the cut $\not{E}_T \geq 75$ GeV. 72

5.3 The uncorrected $\not{E}_T$ distribution of the 107 events passing the cut on corrected $\not{E}_T \geq 75$ GeV. 73

5.4 The detector η distribution of the leading jet for the 3730 events passing the vertex z cut. Events in which the leading jet fell into the region $1.1 < |\eta_{\rm det}| < 1.4$ (bounded by the dotted lines) were rejected. 76

5.5 The definition of the angles $\delta\varphi_k$ used in the jet-$\not{E}_T$ correlation cut. 78

5.6 The correlation of $\delta\varphi_1$ and $\delta\varphi_2$ for events collected by a trigger requiring one jet with $E_T > 20$ GeV; only events with $\not{E}_T > 20$ GeV and three 'good' jets with $E_T > 15$ GeV are included. The lines indicate the boundaries of the regions removed by the cuts listed in section 5.1.6. 80

5.7 The $\not{E}_T$ distribution of the 14 events passing all our analysis cuts. 85

5.8 The $\not{E}_T$ distribution of the JET_MIN data sample, after imposition of jet-$\not{E}_T$ correlation cuts. 94

5.9 The fraction of events passing our three jet requirement as a function of the $\not{E}_T$ of the events. 96

6.1 The signal efficiencies for selected $(m_{\tilde{g}}, m_{\tilde{q}})$ and the fits used in interpolating between them. 103

6.2 The DØ 95% confidence level exclusion contour. The region below the curve is excluded. 107

6.3 Current squark and gluino mass limits. 110

List of Tables

1.1 The gauge and Higgs field content of the MSSM. 10

1.2 The matter field content of the MSSM. 12

3.1 The trigger configurations used in this analysis and their associated integrated luminosities. 44

5.1 The cumulative efficiency for the jet quality cuts as a function of the jet E_T. The error is statistical plus systematic, added in quadrature. 75

5.2 A summary of the cuts used in this analysis and the number of events passing each cut. 84

5.3 Expected backgrounds from W and Z production in association with jets. 90

5.4 The fraction of events satisfying the requirement of three or more jets with $E_T > 25$ GeV as a function of the $\not{E}_T$ of the events. 97

6.1 Squark and gluino production cross sections and detection efficiencies for our 28 simulated event samples. 101

6.2 Our 95% confidence level cross section limit (in picobarns) for the production of gluinos and squarks in $p\bar{p}$ collisions at a center of mass energy of 1.8 TeV, as a function of $m_{\tilde{g}}$ and $m_{\tilde{q}}$. . . . 106

Acknowledgements

In my (many) years as a graduate student, first in residence at Stony Brook and later working at Brookhaven and Fermilab, I have had the great honor of working with many fine people. I'd like to take the time to thank a few of them.

First, many thanks are due to my advisor, Prof. Chang Kee Jung. His high standards have been an inspiration to me. I hope one day to reach them. Many thanks are also due to the entire High Energy Group at Stony Brook. Their support has been invaluable to me, and their enthusiasm for the field is what fired mine.

I'd like to thank the many fine people I worked with at Brookhaven, during the construction of the Central Calorimeter modules, especially Joan Guida. Although she was a Stony Brook postdoc, she put in many long days (weeks, years, ...) in "the factory" at Brookhaven. I will always remember her as the definition of hard-working. I'd also like to thank all the crew who tested, assembled, and debugged the Central Calorimeter at Fermilab. A great deal of effort by many fine people went into that detector; I think our achievement is one we can view with pride. Many thanks are due to all my many colleagues in

the DØ collaboration. Through a great deal of hard (and smart) work we were able to make our first run a great success. Thanks also go to the accelerator staff at Fermilab; without the fruits of their labor our fine detector would be a useless lump of iron and uranium.

I'd like to thank my officemates in the "Stony Brook ghetto"; although it was sometimes difficult to work, it was never boring there.

I'd like to thank the leaders of the New Phenomena group at DØ: the old guard, Nick Hadley and Andy White, who while juggling busy schedules provided exemplary leadership for our group (some much so that Nick was stolen by the toppies); and the new guard, Dave Cutts and Wyatt Merritt, who were able to hit the ground running and keep the operation of the group going smoothly. I don't think we could have had better leadership.

I'd like to thank Howie Baer, who has been an invaluable source of information on SUSY and SUSY phenomenology. He answered all my questions, even the stupid ones, and was always friendly about it. He also made a great translator at SUSY '93.

I'd like to thank the people who helped in the "home stretch" of my thesis preparation. Rich Astur, Dan Claes, Jim Cochran, and Terry Heuring were the finest and most patient group of proofreaders one could hope to find. Thank also to Amber Boehnlein, Wyatt Merritt, and especially Adam Lyon, each of whom was there when I needed the help. I hope all the time Adam put in on tasks for my thesis help him with his, in the not-too-distant future.

Finally, I'd like to thank my family. My wife Laura has suffered, without complaint, for five years as the wife of a graduate student. During the last few

months of my thesis preparation, she has taken care of our children household without my help, and insulated me from any work and worry except for my thesis. Without her love and support I never would have made it. She and our children, Robert and Maria, have often been my only source of joy on many difficult days. I can never thank them enough.

Chapter 1

Introduction

1.1 Symmetry

1.1.1 Symmetries in Physics

The discovery, understanding, and exploitation of symmetries have greatly advanced our knowledge of the physical sciences. Symmetries help us understand physics from a more fundamental basis and provide us with predictive power to extend our theories. They allow us to start with a simple postulate, such as "an absolute position in space is not measurable; only relative positions have meaning," and to deduce from such postulates powerful laws, such as the law of conservation of momentum.

We may group the observed symmetries in physics into four categories [1]

- Symmetries of permutation (interchange of particles). These lead to Fermi-Dirac or Bose-Einstein statistics.

- Symmetries of discrete spacetime transformation. These include the

symmetries of point groups familiar to solid state physicists, and also parity, time reversal, and charge conjugation symmetry.

- Symmetries of continuous spacetime transformation. These include the symmetries of translational and rotational invariance, and of Lorentz invariance.

- Internal (gauge) symmetries. These are the symmetries inherent from the nature of the field associated with a given particle, such as the U(1) associated with electromagnetic charge, or the SU(3) of color.

In particle physics the use of symmetries is pervasive. The Standard Model (SM) [2] is based upon the symmetries which the electromagnetic and weak forces seem to obey; quantum chromodynamics (QCD) is similarly based upon the symmetries observed in meson and hadron spectroscopy. Spontaneous symmetry breaking is invoked to explain the massive vector bosons and the massless photon. The prediction of the W and Z bosons sprang from consideration of symmetries [2]. The discovery of these two particles is one of the great triumphs of modern particle physics [3, 4, 5, 6].

1.1.2 Symmetries of the Standard Model

The Standard Model exhibits permutation symmetry and both types (discrete and continuous) of spacetime symmetry. The SM Lagrangian is invariant under rotations and translations, under Lorentz transformations, and under the product of charge conjugation-parity-time reversal (CPT) transformations.

Each of these symmetries corresponds to some conserved quantity; translational and rotational invariance imply conservation of momentum and angular momentum; the Lorentz invariance implies the conservation of 4-momentum; the invariance under CPT transformations implies that the product of CPT eigenvalues is a conserved quantum number. These symmetries are respected by all the particles of the SM, independent of their internal quantum numbers, and their conservation is believed to be exact.

The gauge (internal) symmetry group of the Standard Model is $SU(3)_C \times SU(2)_L \times U(1)_Y$. The $SU(3)_C$ symmetry is that of the strong (color) interaction; the $SU(2)_L \times U(1)_Y$ symmetry is that of the electroweak sector. We believe the $SU(3)$ of color is unbroken, but the symmetry of the electroweak sector (respected by the primordial $W^{1,2,3}$ and B bosons of the SM) is broken by the Higgs mechanism resulting in the physical $W^{\pm}$ and Z bosons and the massless photon.

Most of the SM has been tested in detail by experiment; those quantities which have been measured to this date have been in agreement with the requirements of the model. In particular, the gauge symmetries of the SM produce predictions in excellent agreement with the available data. There remain, however, some untested aspects of the model.

The spontaneous breaking of the electroweak symmetry by the Higgs mechanism is one of the remaining untested parts of the Standard Model. There is no direct experimental evidence for the existence of the Higgs scalar to this date. The Higgs mechanism also suffers from the 'fine-tuning' problem. In any quantum field theory involving interacting fundamental scalars one

finds that radiative corrections to the scalar mass (δm_H) produce a quadratic divergence in that mass [7]. This divergence is unphysical, because the theory is not applicable for infinite momentum; it breaks down for momenta p that approach the mass scale Λ at which new interactions or new particles, not in the model, become important. For the Standard Model this scale is expected to be that of Grand Unification, giving $\Lambda = \mathcal{O}\left(10^{15}\right)$ GeV. This is the scale at which GUT (Grand Unified Theory) boson exchanges become relevant; such interactions allow the transformation of a quark to a lepton. In any model, the scale of new interactions is presumably less than the Planck scale, $\Lambda = \mathcal{O}\left(10^{19}\right)$ GeV, at which gravitation becomes relevant. Thus the scale Λ actually serves as a cutoff, since physics not contained in the SM becomes important above that scale.

Despite the presence of the 'natural' loop cutoff Λ, the quadratic divergence of the elementary scalar mass still remains a problem. The loop corrections produce a change in the scalar mass given by

$$\begin{aligned} m_H^2 &= m_0^2 + \delta m_H^2 \\ &= m_0^2 - g^2\Lambda^2 \end{aligned} \tag{1.1}$$

where m_0 is the 'bare' Higgs mass parameter and g is a dimensionless coupling parameter. The value of m_H is known to be of the order of the electroweak scale, $\mathcal{O}(10^2)$ GeV. Equation 1.2 then states that if Λ is in fact as large as the Planck scale or even the GUT scale, and if the coupling g is of order unity, then m_0 must be 'tuned' to great precision in order to keep m_H of the correct order of magnitude. While this is not impossible, it is an unpleasant feature

of the SM; the inelegance is compounded by the fact that the tuning must be performed anew for each order in perturbation theory. A method of controlling this divergence other than fine-tuning of parameters would be more pleasing.

We know of three solutions to this problem. One is to introduce a new particle with some interaction which cuts off the loop momentum at a mass scale sufficiently low that loop corrections do not become 'large'. This is unattractive because higher order corrections make still lower bounds on the scale of the new particle or interaction necessary. The second is to make the scalars composite states of some more fundamental fermions. This is the solution used in technicolor theories. The third solution is to introduce a new symmetry that forces the cancellation of the divergence without fine-tuning. Supersymmetry [8, 9, 10] (SUSY) is such a symmetry.

1.1.3 A New Type of Symmetry

Supersymmetry is a symmetry that connects bosons and fermions. It introduces a fermionic partner for every boson (and vice versa) identical in all internal quantum numbers. The connection between bosons and fermions is unique to supersymmetry; all the symmetries listed above provide no such connection.

Supersymmetry is a spacetime symmetry, not an internal symmetry. That is, it can be shown [8] that the anticommutator of the (Majorana spinor) generator Q_α of the supersymmetric transformation satisfies

$$\left\{Q_\alpha, \bar{Q}_\beta\right\} = 2\left(\gamma_\mu P^\mu\right)_{\alpha\beta} \tag{1.2}$$

where P^μ are the generators of the Poincaré group (*i.e.* the generators of Lorentz boosts and rotations) and γ_μ are the Dirac matrices. Because supersymmetry is a spacetime symmetry, it is independent of all internal symmetries; the generator of supersymmetric transformations commutes with the generator of any internal symmetry. This is the reason why the particles in a supermultiplet have the same internal quantum numbers, such as electric and color charge, isospin, lepton number, and so forth.

As stated above, supersymmetry can protect the masses of elementary scalars from quadratic divergences. It is the association of a fermion (which follows Fermi-Dirac statistics) with the elementary scalar (which obeys Bose-Einstein statistics) that protects the mass of the scalar. In an unbroken supersymmetric model, for each diagram in any calculation (such as that of the mass renormalization) containing a scalar loop there is a corresponding diagram containing a fermion loop. Because the couplings of a particle and its superpartner (spartner) are the related, and because the fermion loop introduces a term of opposite sign than that of the boson loop, the fermion and boson contributions cancel exactly order by order in perturbation theory. No tuning of parameters is necessary.

Supersymmetry cannot be an unbroken symmetry in the real world. A bosonic partner to the electron with identical mass, if it existed, would have been detected long ago. Therefore supersymmetry, if present in nature, must be a broken symmetry. Fortunately, it is possible for supersymmetry to be broken without re-introducing quadratic divergences. In order for supersymmetry to still protect the elementary scalar masses the supersymmetry mass

breaking scale must be $\mathcal{O}(10^3)$ GeV.

1.2 The Minimal Supersymmetric Standard Model

1.2.1 Why This Model?

The Minimal Supersymmetric Standard Model (MSSM) [11] is minimal in the sense of being the supersymmetric extension of the Standard Model which has the fewest particles added, while still remaining consistent with the data. It is particularly interesting because, while it is only a model and not a fundamental theory, the MSSM is the low energy limit of several more fundamental theories, for example supergravity Grand Unified Theories (GUTs), or string-inspired supersymmetric models. These theories, if they have sufficient power, may predict (or at least guide us towards) specific ranges for the various parameters which specify the MSSM, such as the particle masses. Therefore the MSSM, although only one model, is in fact quite general and is able to represent a variety of different GUT-scale theories in the energy regime accessible at current or foreseeable future colliders, and is an excellent starting point for experimental searches for supersymmetry.

The MSSM adds to the Standard Model additional Higgs fields and the supersymmetric partner of all the 'normal' particles. Only a few extra parameters, beyond those of the SM, need definition; with the definition of these parameters, all processes in the model are calculable through standard pertur-

bation theory. This includes the cross sections for production and the decay modes of the various sparticles. The model has been proven to be renormalizable.

1.2.2 Gauge and Higgs Field Content

The Higgs sector of the Standard Model includes a single Higgs doublet, which produces one physical (neutral) Higgs boson. The MSSM extends the gauge sector of the SM to include a second Higgs doublet and superpartners for each of the fields of the SM. All particles appear in supermultiplets which combine the 'normal' particles and their partners. Supersymmetry requires that the fields which make up a supermultiplet must have the same number of fermionic and bosonic degrees of freedom. We shall check this in course for the gauge fermions, or gauginos, of the MSSM.

The MSSM gauge and Higgs sector includes three types of particles:

1. the color octet, electrically neutral gluons (massless vector bosons);

2. the color neutral, charged fields: $W^{\pm}$ (massive vector bosons) and $H^{\pm}$ (massive scalars);

3. the color neutral, electrically neutral fields: γ (massless vector boson), Z (massive vector boson), h (light massive scalar), H (heavy massive scalar), and A (massive pseudoscalar).

The superpartners, or *spartners*, of the particles within each of these groups may mix, as long as they share the same quantum numbers. The

simplest case is that of the gluino, the spin 1/2 partner of the gluon. The gluon is the only gauge boson bearing color; therefore the gluino does not mix with any of the other gauginos. Since the gluon field has 16 degrees of freedom (8 color times 2 spin for the massless gluon), the gluino field must also have 16. The gluino is a massive Majorana fermion (there is no distinct antigluon), thus having 8 color times 2 spin degrees of freedom, meeting the required 16 degrees of freedom.

Somewhat more complicated is the case of the charged and neutral vector bosons and Higgs scalars. The $W^{\pm}$ (2 charge times 3 spin = 6 degrees of freedom) and the $H^{\pm}$ (2 charged times 1 spin = 2 degrees of freedom) are matched by two charged, massive fermions, called *charginos*, with a total of 2 particles times 2 charge times 2 spin = 8 degrees of freedom. Since the $W^{\pm}$ and $H^{\pm}$ are both charged, their partners may mix. Only conservation of lepton number prevents the charged leptons from mixing with the charginos as well.

In the neutral gauge boson sector, the massless γ (2 spin degrees of freedom), and the massive Z (3 spin degrees of freedom), h, H, and A (1 spin degree of freedom each) have a total of 8 degrees of freedom; this is matched by the *neutralinos*, a set of four massive Majorana fermions, for a total of 4 particles times 2 spin degrees of freedom = 8 degrees of freedom. Similarly to the charginos, the neutralino mass eigenstates are mixtures of the direct partners of the γ, Z, etc. We shall follow one of the conventional naming schemes, and refer to the charginos and neutralinos by numbered subscripts, with the particles numbered in order of increasing mass. Table 1.1 summarizes the gauge

(and gaugino) field content of the MSSM. Note that the lightest neutralino (the $\tilde{Z}_1$) is in general *not* a pure partner for the photon (photino).

Particle name	Symbol	Spartner name	Symbol
gluon	g	gluino	$\tilde{g}$
charged Higgs	$H^{\pm}$	chargino	$\tilde{W}_{1,2}$
charged weak boson	$W^{\pm}$		
light Higgs	h	neutralino	$\tilde{Z}_{1,2,3,4}$
heavy Higgs	H		
pseudoscalar Higgs	A		
neutral weak boson	Z		
photon	γ		

Table 1.1: The gauge and Higgs field content of the MSSM.

1.2.3 Matter Field Content

The matter content of the MSSM is somewhat simpler than the gauge content. The fundamental matter fermions of the SM are supplemented directly by scalar partners. There is, however, at least one subtlety: the concept of right- and left-scalars. The description right- or left-handed, when applied to a particle with nonzero spin, refers to the direction of the particle's spin with respect to the direction of motion of the particle. A massless particle with nonzero spin, moving at the speed of light, is necessarily either right- or left-handed. A massive particle can exist in a mixture of the two states. A spinless (scalar) particle, however, has no spin to align. This is not the sense in which scalar quarks (squarks) or scalar leptons (sleptons) are right- or left-scalars. The scalar fermions (sfermions), in order to achieve as many degrees

of freedom as their spin 1/2 partners, must appear in two states. These states are the right- and left-scalars, which are the partners of the right- and left-handed fermions. The difference between the two types of scalars is that while left-scalars interact with $W^{\pm}$ bosons (and with the $W^{\pm}$-partner component of the charginos), the right-scalars do not. Both types interact with the Z and the neutralinos, and right-scalars may interact with the $H^{\pm}$-component of the charginos.

The matter field content of the MSSM thus comprises two scalar quarks for each flavor of quark, and two scalar leptons for each flavor of lepton. Left- and right-scalar fermions are nearly degenerate in mass, the degeneracy being broken only by the difference in electroweak interactions. Likewise, the flavors are nearly degenerate, the degeneracy being broken by the difference between the Yukawa couplings of the fermionic partners. This breaking of degeneracy is small due to the large difference between the common squark (or slepton) mass scale and the masses of the known quarks and leptons. The case of the top quark sector may be different. Because of the large mass of the top quark, the mixing between the right- and left- components of the scalar top may not be small. This leads to the formation of mass eigenstates that are mixtures of the two, commonly denoted $\tilde{t}_1$ and $\tilde{t}_2$, with the former being lighter than the latter. In this thesis, we do not deal with the model-dependent details of the scalar top sector. Table 1.2 summarizes the matter field content of the MSSM.

Particle name	Symbol	Spartner name	Symbol
quark	q	squark	$\tilde{q}_{R,L}$
lepton	l	slepton	$\tilde{l}_{R,L}$

Table 1.2: The matter field content of the MSSM.

1.2.4 Parameters of the MSSM

One of the attractive features of the MSSM is that there are only a few parameters (in addition to those of the SM) which need specification before all masses and couplings are defined, and calculations may be performed. There is more than one way to select which set of parameters are to be considered as 'fundamental'. Influenced by our chosen Monte Carlo event generator, we choose the following as our set of fundamental quantities:

- $m_{\tilde{g}}$, the gluino mass (this sets the scale for all gauginos);
- $m_{\tilde{q}}$, the common squark mass (this sets the scale for all scalar fermions);
- $m_{H^{\pm}}$, the charged Higgs mass (this sets the scale of all Higgs masses);
- μ, the higgsino mass mixing parameter (this determines the gauge content of each of the charginos and neutralinos);
- $\tan(\beta)$, the ratio of vacuum expectation values of the two Higgs doublets.

Once these parameters are specified, the masses of all other particles, as well as their couplings, are set. Note that we have neglected, in this specification, several additional parameters which influence the top sector, and also that

we have chosen to have the slepton mass equal to the squark mass. This is not required by the MSSM, and each supersymmetric GUT has its own requirement on the ratio of the slepton and squark masses. We shall return to this point after discussing the decay of supersymmetric particles.

1.2.5 R-Parity Conservation

The gauge interactions of the MSSM Lagrangian allow for the definition of a new multiplicative quantum number R, which may be chosen to be $+1$ for 'normal' particles, and -1 for 'supersymmetric' particles. It is also possible to define R as

$$R = (-1)^{3(B-L)+2S} \tag{1.3}$$

where B is the baryon number, L is the lepton number, and S is the spin of the particle. Although it is possible to construct models in which R is not conserved, any R-parity violating terms in the Lagrangian also violate lepton or baryon number conservation.

In the MSSM, R is a conserved quantum number, with the result that $R = -1$ particles (the sparticles) must always be pair produced, and that the lightest supersymmetric particle (LSP) is absolutely stable. Furthermore, the decay products of each supersymmetric particle must include an odd number of supersymmetric particles, and all decay chains must end with one LSP. Since we have not yet discovered a suitable candidate for the LSP, and also because of cosmological constraints, the LSP must be electrically and color neutral; it may interact only weakly or gravitationally.

1.2.6 Determining the Mass Spectrum

In the MSSM, the lightest neutralino (the $\tilde{Z}_1$) is generally taken to be the LSP. Although the possibility that the scalar neutrino (or sneutrino, $\tilde{\nu}$), which is also uncharged and interacts only through gravitation and the weak interaction, may be the LSP is not completely ruled out, cosmological constraints make it disfavored. Existence of the $\tilde{\nu}$ as the LSP is ruled out for $m_{\tilde{\nu}} < 1.4$ TeV [12].

The values of the parameters $\tan(\beta)$, μ, and the masses $m_{\tilde{g}}$ and $m_{\tilde{q}}$ determine the masses of the gauginos and also the gauge field content of the mass eigenstates, which in turn determines their coupling strengths. To reduce the number of arbitrary parameters in the model we assume the soft supersymmetry breaking gaugino masses are related to the gauge couplings as in supergravity GUT models. Our choice of degenerate squark masses (except for the scalar top) is also motivated by supergravity GUT models in which all squark masses are degenerate at the GUT scale; in these models breaking of the degeneracy is small except for the scalar top.

1.3 Squarks and Gluinos in the MSSM

1.3.1 Production of Squarks and Gluinos in $p\bar{p}$ Collisions

As stated above, sparticles must always be produced in pairs. Because they couple via the strong force squarks and gluinos would be the most copi-

ously produced sparticles in any hadron collider, assuming the collider energy is sufficiently high to make such particles. There are many possible diagrams for the production of squarks and gluinos. These are analogous to the many quark and gluon production diagrams possible. The three possible reactions are gluino pair production, squark pair production, and associated (gluino and squark) production. The relative magnitudes of these processes are determined primarily by the relative masses of the squark and gluino. Neutralinos and charginos, as well as sleptons, would also be produced in $p\bar{p}$ collisions, via electroweak interactions, and can produce interesting signatures. In this analysis, we consider only the strong production of squarks and gluinos.

1.3.2 Decay Modes of Squarks and Gluinos

The decay of squarks and gluinos in the MSSM can be quite complex, since the gaugino spectrum of the model is quite rich [13, 14]. The details of the decay modes for squarks and gluinos depend quite strongly upon the mass spectra and also the gauge field content of the neutralinos and charginos, which in turn depend on the five input parameters of the model. Nevertheless, a few generalizations may be made. Left-squarks can decay both through charginos and neutralinos, but right-squarks may decay only through neutralinos. This means that right-squarks often produce fewer jets in the final state than left-squarks. If the gluino mass is less than the squark mass, both right- and let-squarks can decay into a quark and gluino; this decay is generally favored if it is allowed. The gluino can also have many decay modes, depending upon

whether the squark is lighter or heavier than it.

1.3.3 Signatures of Squark and Gluino Decay

Since the LSP is present in the decay of all supersymmetric particles, its detection would be one of the clearest signatures for supersymmetry. Since the LSP interacts only weakly or gravitationally its detection in a collider detector is not possible; instead, the signature of the LSP is missing transverse energy ($\not{E}_T$). In older supersymmetric models (those which did not consider the mixing of the sparticles in the gaugino sector to be significant) squarks and gluinos were expected to decay directly to quarks and the LSP. The $\not{E}_T$ signature for a heavy squark or gluino in such a direct decay model could be quite spectacular. The presence of the cascade decays in the current MSSM weakens this signature by softening the $\not{E}_T$ spectrum of both squark and gluino production events [15]. These same cascade decays can also lead to a large number of quarks, leptons, or both in the final state, thus making multiple jets or leptons another significant signature for squark and gluino production. In this analysis, we look for the signature of large $\not{E}_T$ and multiple jets.

1.4 Why Do this Search?

Supersymmetry is an elegant theory which suffers one embarrassing question: where are the particles? Experimenters began to search for supersymmetric particles soon after the introduction of the theory, but to this date there has been no positive signal seen. Lower limits have been set on the masses

of many of the particles of many different supersymmetric models; no model has been verified. Nevertheless, recent measurements by the LEP experiments of the running of the coupling constants have exhibited consistency with one class of supersymmetric GUT, and indicate a mass scale for supersymmetric symmetry breaking of $\mathcal{O}(10^3)$ GeV [16]. The Tevatron is now and shall remain for many years the highest energy accelerator in world. It provides an exciting theater for the search for supersymmetric particles.

Chapter 2

The Apparatus

The DØ detector has been constructed to study $p\bar{p}$ collisions at a center of mass energy of 1.8 TeV in the Tevatron at the Fermi National Accelerator Laboratory in Batavia, Illinois. The detector is named for its location, the DØ interaction region, which is one of the two high-luminosity beam crossing locations in the Tevatron.

2.1 The Tevatron

The Tevatron is the highest energy particle collider in the world today. It collides protons and antiprotons ($p\bar{p}$ collisions) at a center of mass energy ($\sqrt{s}$) of 1.8 trillion electron-volts (1.8 TeV). In some of the collisions, the constituents which make up the proton and antiproton interact violently; in the process, new particles are created, many of which are seen (on Earth, at least) only in such collisions. It is for the study of such interactions, and such particles, that the Tevatron and its two collider detectors, CDF and DØ, were

Chapter 2

The Apparatus

The DØ detector has been constructed to study $p\bar{p}$ collisions at a center of mass energy of 1.8 TeV in the Tevatron at the Fermi National Accelerator Laboratory in Batavia, Illinois. The detector is named for its location, the DØ interaction region, which is one of the two high-luminosity beam crossing locations in the Tevatron.

2.1 The Tevatron

The Tevatron is the highest energy particle collider in the world today. It collides protons and antiprotons ($p\bar{p}$ collisions) at a center of mass energy ($\sqrt{s}$) of 1.8 trillion electron-volts (1.8 TeV). In some of the collisions, the constituents which make up the proton and antiproton interact violently; in the process, new particles are created, many of which are seen (on Earth, at least) only in such collisions. It is for the study of such interactions, and such particles, that the Tevatron and its two collider detectors, CDF and DØ, were

built.

A detailed description of the Tevatron may be found elsewhere [17]; here we describe it but briefly. Figure 2.1 shows the layout of the Tevatron and its associated accelerators. The starting point for producing the colliding beams

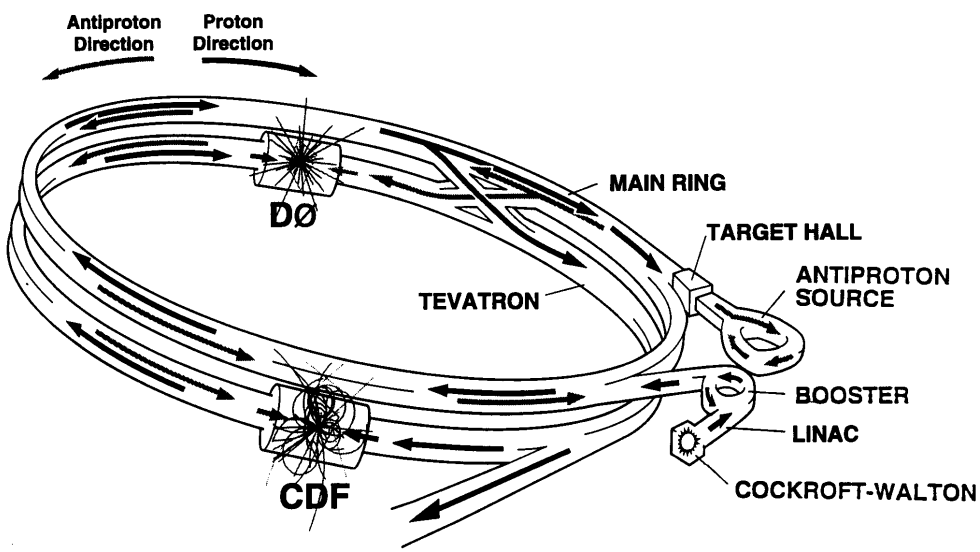

Figure 2.1: A schematic layout of the Tevatron and its associated accelerators.

is a Cockcroft-Walton accelerator which propels a beam of H^- ions to an energy of 750 keV. The ions are then injected into a linear accelerator, the Linac, where they are accelerated to an energy of 200 MeV. There they are shot through a carbon foil to strip off the electrons, leaving a beam of H^+ ions, which are bare protons. The protons are next sent into a synchrotron (the Booster) which accelerates them to 8 GeV. From the Booster the protons are injected into a larger synchrotron, the Main Ring. The Main Ring resides in an underground tunnel and is 3.7 miles in circumference. In the Main Ring

the protons are accelerated up to 120 GeV. Some of the protons are injected into the Tevatron, and some are extracted to begin the production of the antiproton ($\bar{p}$) beam.

The extracted protons are collided into a copper and nickel target. This collision produces antiprotons; for every million protons incident, about 20 antiprotons are collected in the next step of the production process. The antiprotons are produced with a wide range of momenta; they are focused and stored in a pair of storage rings, where the beams are 'cooled', that is, the antiprotons are brought into orbits with a much smaller range of momenta. When enough antiprotons have been accumulated, they are injected into the Main Ring, and accelerated to 150 GeV; they are then injected into the Tevatron in the direction opposite to the proton beam.

The Tevatron is in the same tunnel as the Main Ring and has the same 3.7 mile circumference. It contains superconducting magnets and can achieve greater magnetic fields and thus greater beam energies. In the Tevatron, the beams are accelerated to 900 GeV. Along the Tevatron ring are two high-luminosity collision regions, called B0 and D0. At these locations, the beams are collided and studied by the collider detectors: CDF located at B0, and DØ, located at D0.

2.2 The DØ Detector

The DØ detector is a general purpose collider detector. It is optimized for high p_T physics, for identification of both muons and electrons over a large

solid angle, and for good jet and missing transverse energy measurement ($\not{E}_T$). Figure 2.2 shows a cutaway view of the DØ detector.

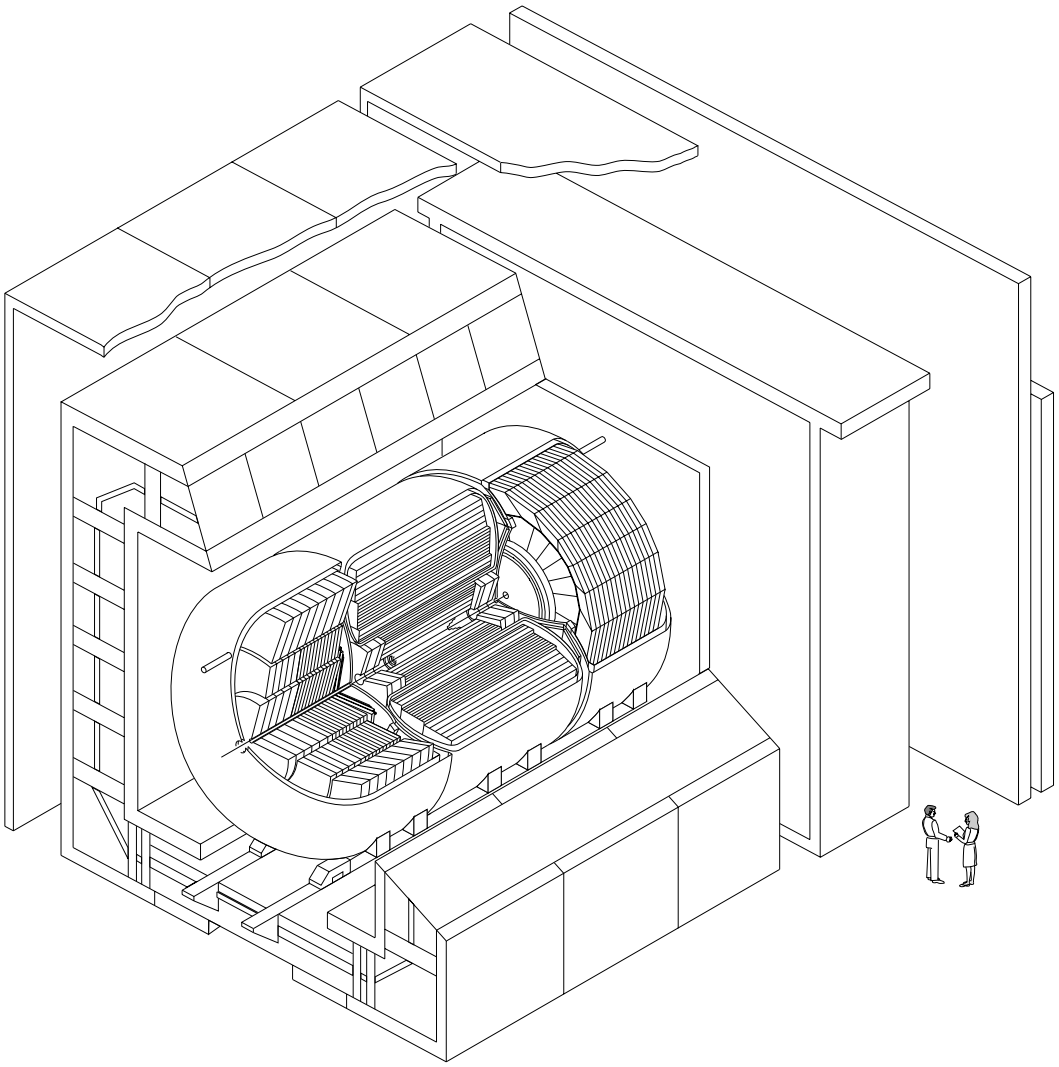

Figure 2.2: An isometric cutaway view of the DØ detector.

The detector consists of three nested shells. The innermost shell contains the central tracking and transition radiation detectors; surrounding these is the calorimeter, and surrounding the calorimeter is the muon detector. Of

primary importance in this analysis is the hermeticity of the calorimetry, which is crucial for good measurement of $\not{E}_T$. A detailed description of the detector is available in reference [18] and references therein; in this chapter we give a brief overview of the detector elements.

2.2.1 The DØ Coordinate System

For uniformity of description the DØ Collaboration has defined a standard coordinate system; this system shall be used throughout this dissertation. The system defines $+\hat{x}$ to be a unit vector pointing radially outward from the center of the accelerator ring, $+\hat{y}$ to be a unit vector pointing up, and $+\hat{z}$ to be orthogonal to both such that the system is right-handed; this direction is also called 'south'. Protons from the accelerator move in the $+\hat{z}$ direction, and antiprotons in the $-\hat{z}$ direction. We also frequently use a spherical coordinate system, with the polar angle ϑ defined as the angle from the $+\hat{z}$ axis, and the azimuthal angle φ defined as the angle around the $+\hat{z}$ axis with $\varphi = 0$ being the $+\hat{x}$ direction and $\varphi = \pi/4$ being the $+\hat{y}$ direction. Commonly used in place of ϑ is the pseudorapidity η, defined as $\eta = -\ln(\tan(\vartheta/2))$. The pseudorapidity is a convenient variable for $p\bar{p}$ collider physics; for massless particles it is the same as the Lorentz invariant rapidity y, defined by $y = \frac{1}{2}\ln((E + p_z)/(E - p_z))$.

2.2.2 Central Tracking

The DØ central tracking volume contains no magnetic field. This design was chosen to make the chambers compact, so that DØ could have a

hermetic calorimeter at a reasonable cost. The goal of the central tracking system is therefore not the reconstruction of momenta, but rather aiding in the identification of leptons in the calorimeter and muon system. The tracking chambers also find the location of the primary interaction vertex so that directed energy vectors in the calorimeter may be reconstructed correctly. The design has been optimized to maximize two-track resolution, to obtain high efficiency, and to obtain good ionization energy measurement to distinguish single electrons from conversion pairs. The central tracking system comprises four detector subsystems; the Vertex Drift Chamber (VTX), the Central Drift Chamber (CDC), the two Forward Drift Chambers (FDC), and the Transition Radiation Detector (TRD). The VTX, CDC and TRD are arranged in concentric cylindrical shells surrounding the beam pipe and covering the central region. The FDCs are positioned perpendicular to the beam pipe, one at each end of the central tracking volume. Figure 2.3 shows the side view of the complete central tracking system.

VTX

The VTX chamber is the innermost tracking detector in DØ. The purpose of the VTX chamber is to allow the accurate reconstruction of the location in z of the interaction vertex. The inner radius of the VTX is 3.7 cm; the outer radius is 16.2 cm. The total length of the active region is 116.8 cm. The device consists of three concentric layers of cells. The cells are azimuthal sections which span the length of the detector in the z direction. The innermost layer has 16 cells; the other two each have 32. Each cell contains eight sense

Figure 2.3: A side view of the DØ Central Tracking detectors.

wires to determine the φ coordinate of each hit. Adjacent sense wires are staggered by 0.1 mm to resolve left-right ambiguities. The gas chosen for the operation of the chamber is a mixture of CO_2 (95%) and ethane (5%) with a small admixture of water at one atmosphere. The gas is unsaturated at the operating condition of the chamber. The VTX chamber was not used for vertex reconstruction in this analysis.

TRD

The TRD is located between the shells of the VTX and the CDC. The purpose of the TRD is to identify electrons in a manner independent of the calorimeter. A π^0 decaying to two unresolved photons overlapped by a charged

track such as that of a low energy $\pi^{\pm}$ looks to the calorimeter and drift chambers much like an electron; the TRD is used to determine the $\beta\gamma$ of the charged object to distinguish low energy charged particles overlapped by an energetic neutral pion from high energy electrons. The TRD was not used in this analysis.

CDC

The CDC is a cylindrical shell surrounding the TRD and the VTX chamber. The CDC has three purposes: to find the z location of the interaction vertex or vertices, to provide tracks to distinguish between electrons and photons found in the calorimeter, and to aid in the identification and momentum measurement of muons seen in the muon detector. It is 184 cm in length, with an inner radius of 49.5 cm and an outer radius of 74.5 cm. The chamber consists of a single ring of 32 modules. Each module contains four layers. The cells of each layer are staggered in φ with relation to those in adjacent layers to aid in the resolving of left-right ambiguity in the location of hits. Each cell spans two modules. Figure 2.4 shows the layout of one CDC module. Each cell contains seven sense wires and two delay lines, with the delay lines situated radially inward from the first and radially outward from the last of the sense wires. Each delay line is read out from both ends; the sense wires are all read out from one end. Adjacent sense wires are staggered by 0.2 mm to further help resolve left-right ambiguity in the location of hits. The gas used in the CDC is a mixture of Ar (92.5%), methane (4%), and CO_2 (3%) with 0.5% water vapor, at a pressure of one atmosphere.

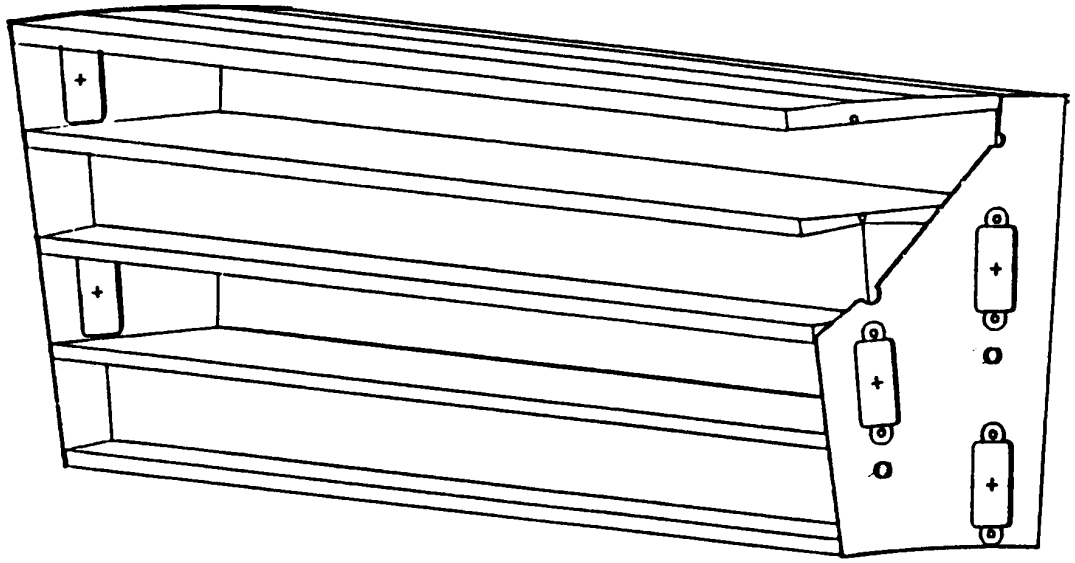

Figure 2.4: An isometric view of one of the 32 Central Drift Chamber modules, showing the staggering of cells between layers and the spanning of modules by cells.

FDC

The FDC consists of two identical sets of disks, oriented with their axes parallel to the beam direction. One is located at the north end of the CDC, and one at the south. Figure 2.5 is a diagram of one of these sets of disks. The purpose of the FDC is the same as that of the CDC; together with the CDC, the FDC extends the tracking down to 5° from the beampipe. There is a small gap between the outer radius of the FDC and the CDC to allow cables from the inner detectors to exit the detector.

Each of the FDCs consists of a stack of three chambers; there is one Φ chamber, with radial sense wires to determine the azimuthal coordinate of each hit, sandwiched by two Θ chambers, which measure (approximately) the polar

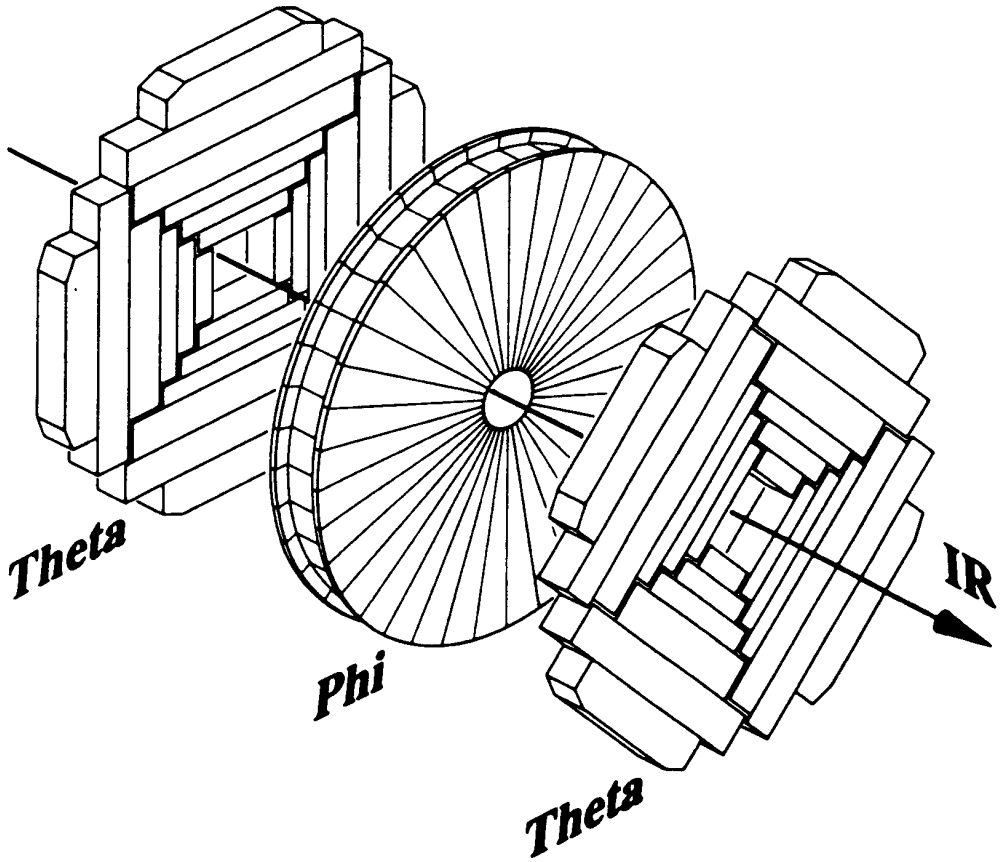

Figure 2.5: An exploded isometric view of one DØ Forward Drift Chamber.

angle of each hit. The Φ chamber contains 36 segments each with 16 sense wires and covers the full range of azimuth. Each of the Θ chambers is made of four independent quadrants. Each of the quadrants contains six rectangular cells, with each cell's long axis tangent to circles of increasing radii about the beam axis. The FDC uses the same gas mixture as the CDC.

2.2.3 Calorimeters

The heart of the DØ detector is a finely segmented uranium-liquid argon sampling calorimeter. The theory of sampling calorimeters is described well in the literature [19]; here we merely present the specifics of the DØ calorimeter.

The calorimeter is housed in three cryostats, one each for the Central Calorimeter (CC), and the North and South End Calorimeters (ECN and ECS). In the space between the calorimeters is deployed a set of scintillating tiles and associated phototubes called the Intercryostat Detector (ICD). Each of the calorimeters is divided into electromagnetic and hadronic layers; the electromagnetic layers are optimized for the identification and measurement of electrons and photons and the hadronic layers are optimized to contain and measure jets. Figure 2.6 shows the layout of the three cryostats, the location of the calorimeter modules within the cryostats, and the location of the central detectors in relation to the calorimeters. Figure 2.7 is a side view of one quarter of the full calorimeter. It shows the transverse and longitudinal segmentation of the calorimeter, the locations of the CC, EC, and ICD, and the relative locations of the central tracking detectors. It also shows the location of the

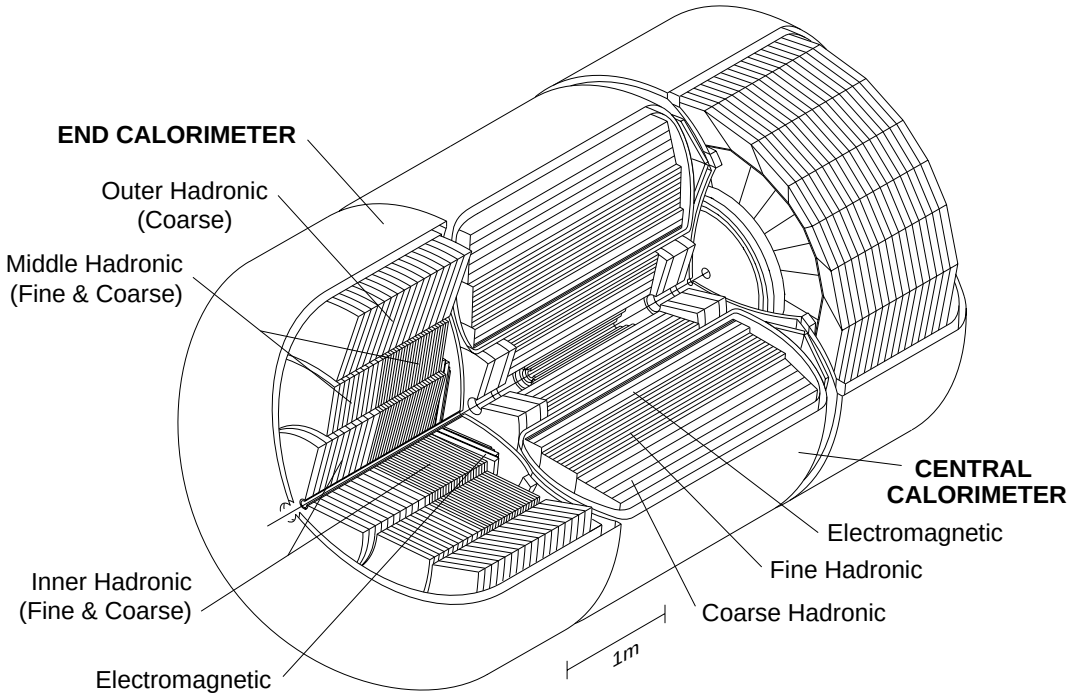

Figure 2.6: An isometric view of the DØ calorimeters

Main Ring bypass, which passes through the Coarse Hadronic section of all three calorimeters.

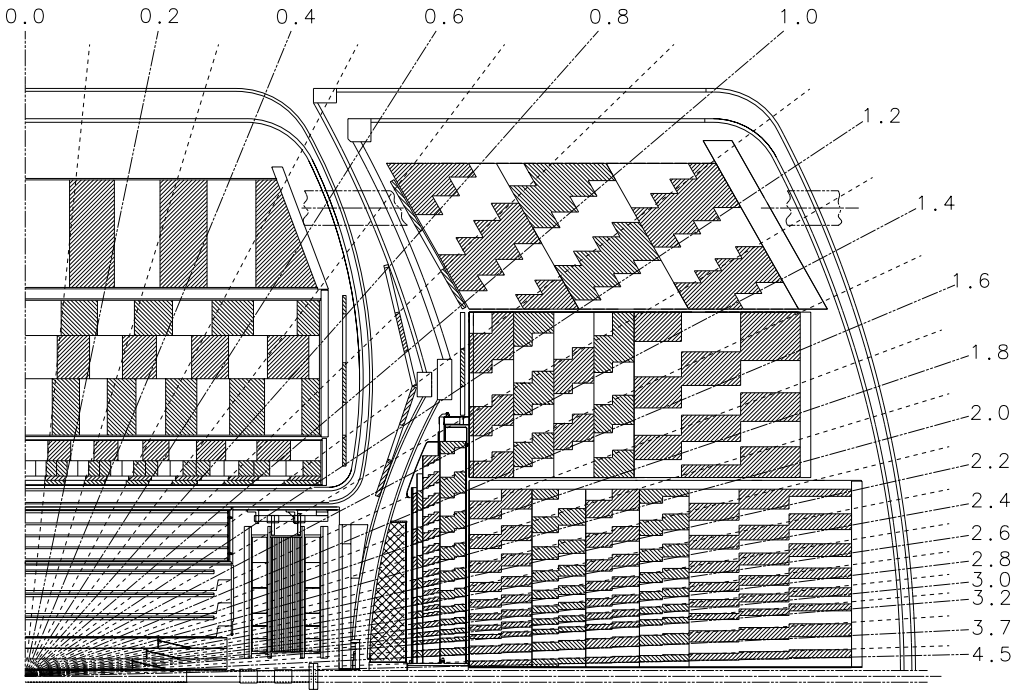

Figure 2.7: A side view of one quarter of the DØ calorimeters and central tracking detectors. Shown alternately shaded and unshaded are the semiprojective towers, and their transverse and longitudinal segmentation. The numbers are the pseudorapidity η at each tower boundary. Also shown is the Main Ring Bypass tube (the horizontal tube at the upper right) and the ICD scintillator tiles, located on the inner face of the end cryostat.

Central Calorimeter (CC)

The Central Calorimeter (CC) resides in the center most cryostat, and covers the region $|\eta| \leq 1.2$ It consists of three concentric rings of three different kinds of modules. Closest to the interaction region are 32 CC Electromagnetic modules (CCEM); around these are 16 CC Fine Hadronic modules (CCFH),

and around these are 16 CC Coarse Hadronic modules (CCCH). Each module is finely segmented in both the transverse and longitudinal directions. The transverse segmentation is typically 0.1×0.1 in $\eta \times \varphi$. The segmentation is finer in CCEM at the depth of the electromagnetic shower maximum. The longitudinal segmentation is different for each of the modules. The energy deposit in each of these segments, or *cells*, is read out independently.

CC Electromagnetic Calorimeter (CCEM)

The CCEM calorimeter has a thickness of 21 radiation lengths. The 32 modules each cover the full length in z and ≈ 0.2 radians in azimuth. These modules are divided into four readout depths which are two, two, seven, and ten radiation lengths thick, respectively. The third layer covers the depth at which the maximum of the EM shower is located. This layer has transverse segmentation of 0.05×0.05 in $\eta \times \varphi$; the other layers have the normal segmentation.

Several of the CCEM modules were exposed to a testbeam at Fermilab. The energy resolution for electrons in the CCEM modules has been found to be of the form

$$\left(\frac{\sigma}{E}\right)^2 = C^2 + \frac{S^2}{E} + \frac{N^2}{E^2} \tag{2.1}$$

where the constants C, S, and N represent calibration uncertainties, sampling errors, and noise contributions, respectively, to the energy resolution and E is the energy of the incident electron. For electrons in CCEM the measured values of these constants are $C = 0.003 \pm 0.004$, $S^2 = (0.162 \pm 0.011)^2$ GeV,

and $N = 0.140$ GeV [20].

CC Hadronic Calorimeter (CCFH and CCCH)

The electromagnetic calorimetry is backed up by a thick hadronic calorimeter. In the Central Calorimeter the electromagnetic section is about 0.8 interaction lengths thick and is followed by a total of 6.4 interaction lengths of hadronic calorimetry. This thickness is divided into four depths and covers the range $|\eta| \leq 0.9$.

The 16 fine hadronic (CCFH) modules, like the CCEM modules, have uranium as their absorber material. The transverse segmentation is again 0.1×0.1 in $\eta \times \varphi$ and the three depths are 1.3, 1.0, and 0.9 interaction lengths thick. The CCFH ring is oriented so that none of the intermodule boundaries of the CCEM ring align with any of those of the CCFH ring.

To fully contain most jets, the CCFH modules are backed up by a coarse hadronic (CCCH) leakage calorimeter. The CCCH modules have copper plates, rather than uranium, as their absorber material. The 16 CCCH modules have transverse segmentation the same as the CCFH modules and longitudinal segmentation of a single depth of 3.2 interaction lengths. The CCCH ring is oriented so that none of the CCFH intermodule boundaries coincide with any in CCCH.

End Calorimeter (EC)

The two End Calorimeters are of identical construction to each other. Like the Central Calorimeter, each consists of a finely segmented electromag-

netic layer, followed by both fine hadronic calorimetry and a coarse (leakage) hadronic calorimetry. Each contains a single electromagnetic module backed by hadronic calorimetry in the form of a single large module surrounded by two rings each of 16 smaller modules.

EC Electromagnetic Calorimeter (ECEM)

To prevent loss of electron acceptance due to projective cracks the ECEM modules were each made a single monolithic module. Each module is a disk, with the axis of the disk coinciding with the Tevatron beampipe. The coverage of each ECEM module is from η of ± 1.4 to ± 4.0. Each module is divided into four longitudinal segments of 0.3, 2.6, 7.9, and 9.3 radiation lengths. The material of the cryostat walls brings the total absorber thickness of the first layer to about 2.0 radiation lengths. As in the CCEM modules, the third layer of ECEM is transversely segmented into 0.05×0.05 cells in $\eta \times \varphi$; beyond $|\eta| = 2.6$ this increase in segmentation is not present because of the small physical size of the cells.

The energy resolution of electrons in ECEM was measured to be (following Equation 2.1) $C = 0.003 \pm 0.003$, $S^2 = (0.157 \pm 0.006)^2$ GeV, $N = (0.29 \pm 0.03)$ GeV. [21].

EC Hadronic Calorimeter (ECIH, ECMH and ECOH)

One EC Inner Hadronic (ECIH) module resides behind each of the ECEM modules and, like the ECEM modules, the ECIH are disks with the Tevatron beampipe passing through the axis of the disks (see Figure 2.7). Each has five

longitudinal sections, four fine hadronic sections with 1.1 interaction lengths of uranium as absorber, and a single coarse hadronic section with 4.1 interaction lengths of stainless steel as absorber.

The EC Middle Hadronic (ECMH) and EC Outer Hadronic (ECOH) modules are arranged in rings around the beampipe, and are cylindrical wedges, like the Central Calorimeter modules. Each of the ECMH modules has four longitudinal segments of 0.9 interaction lengths of uranium absorber, backed by a coarse hadronic section with stainless steel absorber which is 4.4 interaction lengths thick. Each ECOH module consists of a single longitudinal segment with stainless steel absorber plates and is about seven interaction lengths thick. The plates of the ECOH modules are inclined at an angle of approximately 60° with respect to the beampipe.

The hadronic coverage of the End Calorimeters extends from the region covered by the Central Calorimeter out to $|\eta| = 4.45$. The transverse segmentation of the EC hadronic modules is 0.1×0.1 in $\eta \times \varphi$ for all $|\eta|$ up to 3.2 at which point the small physical size of such towers required increasing the φ segmentation to 0.2. The η segments are also larger (and of varying size) for the most extreme values of η.

In the DØ testbeam the response of the ECMH modules to pions was measured to be of the form of Equation 2.1, with $C = 0.047 \pm 0.005$, $S^2 = (0.439 \pm 0.042)^2$ GeV, and $N = 1.28$ GeV [20].

Intercryostat Detector (ICD)

In the regions between the central and each of the end calorimeter cryostats, we have instrumented the cryostat faces with arrays of scintillating plastic tiles, called the Intercryostat Detector (ICD). This was done to keep the resolution of the calorimeter as uniform as possible, even across the regions where the presence of the cryostats introduces the greatest amount of dead material. Figure 2.7 shows the location of the ICD.

Each ICD consists of 384 scintillation tiles of size 0.1×0.1 in $\eta \times \varphi$, to match the cell size of the liquid argon calorimeters. Additional single cell devices called 'massless gaps' were installed in both the CC and EC to instrument the otherwise dead material of the CCFH endplates and the inner wall of the EC cryostat.

2.2.4 Muon Detector

The DØ muon detector consists of three superlayers of proportional drift tubes (PDTs), to detect the passage of charged particles, and a set of iron toroid magnets, to allow measurement of the momentum of particles traversing the detector. Figure 2.8 is a cross section view of the entire DØ detector, showing the location of each of the toroids, the superlayers, and the calorimeters and central detector within. In this analysis, the muon system was used to identify and reject events containing one or more muons from the interaction region. Therefore momentum resolution is less important than coverage of as much solid angle as possible. Also important is the extreme thickness of

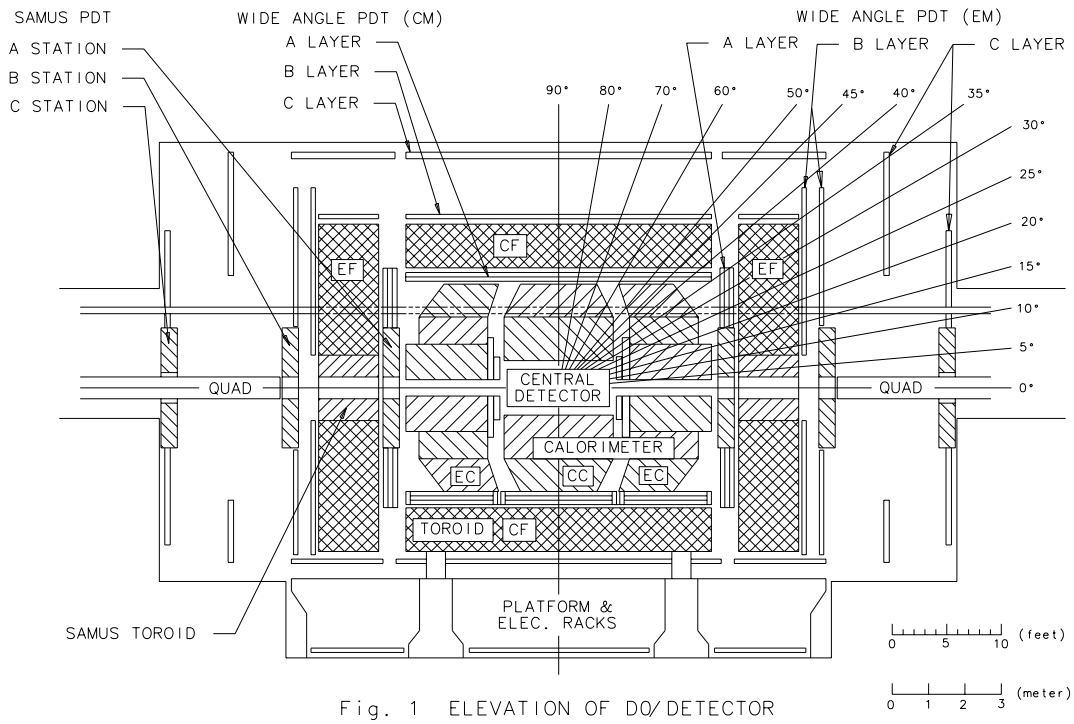

Figure 2.8: A side view of the DØ detector showing the full muon system.

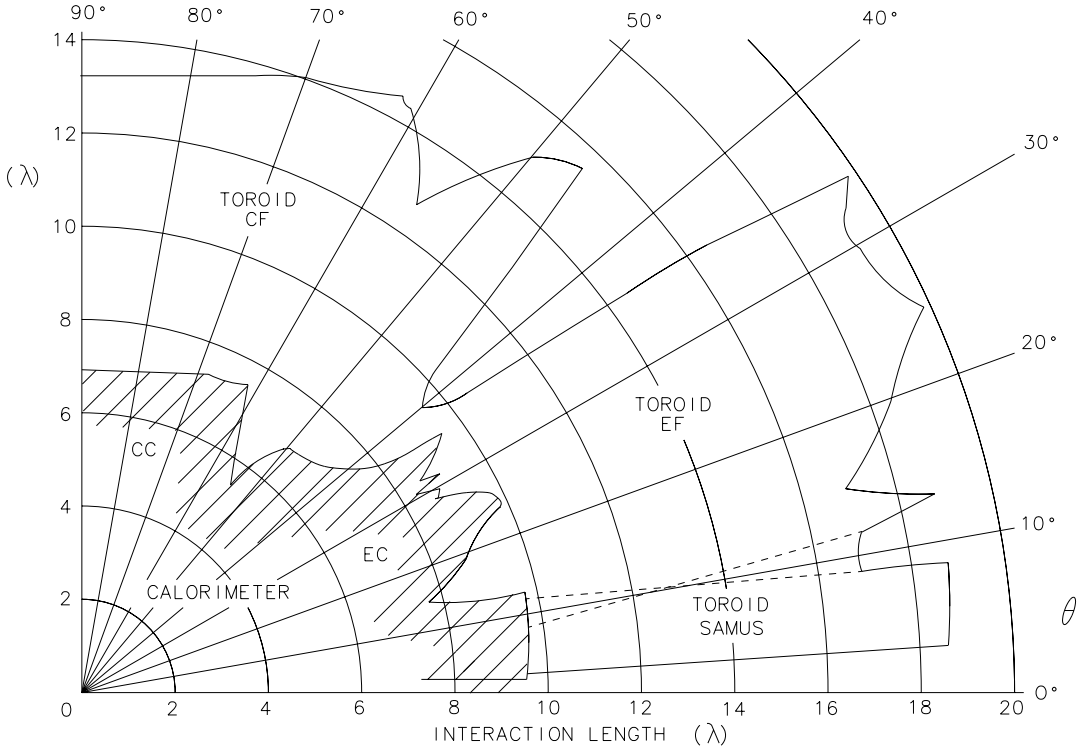

Figure 2.9: The thickness of the DØ detector, in nuclear interaction lengths, as a function of the polar angle ϑ.

the calorimeter and the muon toroids which makes the likelihood of hadronic punchthrough very small, thus allowing measurement of muons within jets. The muon system coverage extends down to approximately 3 degrees from the beampipe, and the thickness of the detector (before the outer layer of PDTs) is typically more than 12 nuclear interaction lengths. The thickness profile of the DØ detector is shown in Figure 2.9. The central region of the detector (CF) covers the range of pseudorapidity $|\eta| < 1.0$; the end toroids (EF) extends this coverage to $|\eta| < 2.5$. Together these two regions form the Wide Angle Muon System (WAMUS). The WAMUS PDTs are distributed into three superlayers.

Inside the toroids is the A layer, which contains four planes of PDTs. Outside the magnet are the B and C layers, each containing three planes of PDTs. The B and C layers are separated by about one meter, to provide a lever arm for momentum measurement. Adjacent planes of PDTs within each layer are offset to help eliminate the left-right ambiguity associated with hit finding in drift tubes.

The PDTs are oriented such that the bend direction of the magnets matches the direction of greatest accuracy of position measurement. The non-bend coordinate, along the length of the wire, has less accuracy; the hit location along the length of the wires is determined by a combination of timing and pad signals.

The Small Angle Muon System (SAMUS) detector extends the coverage for detection of muons to $|\eta| = 3.6$. The design and functioning of the SAMUS is similar to that of the WAMUS although the high hit occupancy of the forward regions forces the use of smaller drift tubes than in the central region.

2.2.5 Trigger

A detailed description of the DØ trigger system may be found in the literature [22, 23, 24]; here we give only a brief introduction. The DØ trigger system comprises three tiers. A hardware trigger (Level 0 or LØ) recognizes that a collision has occurred. A second hardware trigger (Level 1 or L1) requires localized deposits (single tower, electromagnetic only or both hadronic and electromagnetic) or global energy sums (scalar E_T or $\not{E}_T$) above given

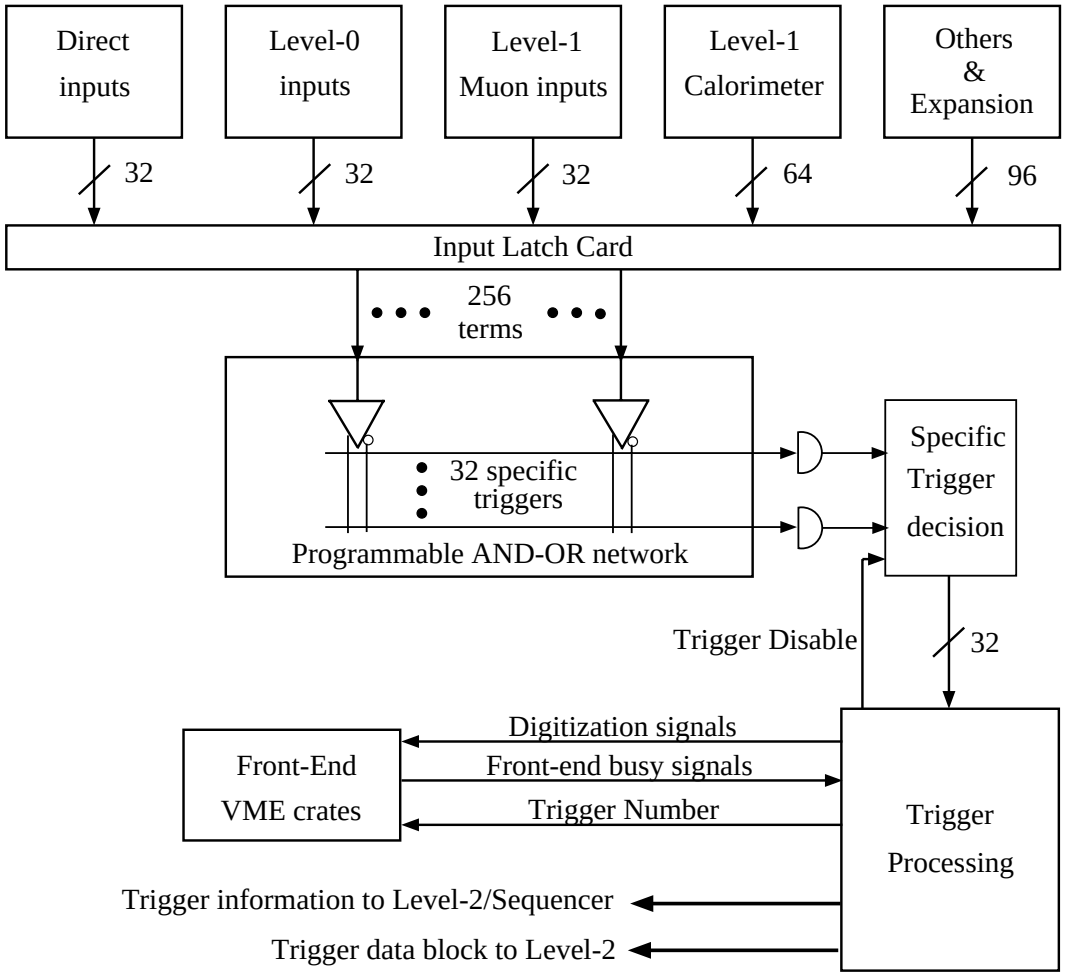

Figure 2.10: A schematic diagram of the DØ data acquisition and trigger system.

thresholds, or simple patterns of hits in the muon chambers that indicate a possible charged particle track. A software trigger (Level 2 or L2) performs detailed event reconstruction to identify interesting events. There is also a Level 1.5 system used for some muon triggers; this system was not used in any of the triggers employed in this analysis. Figure 2.10 is a schematic diagram of the DØ data acquisition (DAQ) and trigger system.

Level 0

The LØ trigger consists of a set of scintillators located between the FDC and the adjacent EC to detect the particles resulting from a hard interaction. LØ is more than 99% efficient at detecting non-diffractive inelastic collisions within the detector.

Level 1

The L1 trigger consists of both calorimeter and muon trigger hardware. No L1 muon triggers were used in this analysis.

The L1 calorimeter trigger system is activated when it receives from LØ the signal that a collision has occurred. The detector crates are read out, with the analog signals traveling along two paths. One path is the 'trigger pickoff' path and the other is the 'precision readout' path. The trigger pickoff path is used to quickly determine the approximate energy in each of the calorimeter cells; the cells are summed into trigger towers which are 0.2×0.2 in $\eta \times \varphi$. The E_T deposits in a given trigger tower are computed using a lookup table based on the LØ estimate of the z location of the interaction vertex. Electromagnetic cells are summed separately from hadronic cells. The $\not{E}_T$ and scalar E_T are also determined from the tower quantities.

The tower transverse energies, $\not{E}_T$, and scalar E_T are compared to the requirements specified in the current *trigger menu.* A trigger menu is a software specification of what conditions, such as a given number of trigger towers with E_T above a given threshold, must be met to satisfy a trigger. The L1

system allows a menu of 32 distinct 'specific triggers'. If one or more of the triggers are satisfied L1 tells the detector electronics crates to begin digitizing the event. The L1 decision must be made within 2.2 μs to allow sufficient time to reset the front end electronics before the next beam crossing.

Level 2

After the crates have digitized an event, the data is sent to a farm of 48 Microvax 4000/60 computers which make up the Level 2 (L2) filter system. Here partial event reconstruction is done, to find jets, electrons, photons, or muons, or to make better calculation of the $\not{E}_T$ and scalar E_T. Many different (up to 128 at one time) software filters can run in the L2 nodes, each connected to one of the L1 triggers. A given event goes to a single L2 node where all the appropriate filters, as defined by the current trigger menu and the L1 trigger that passed the event, are run. If any of the filters pass the event, it is sent to the DØ Host computer where it is written to tape.

Chapter 3

Data Collection and Processing

One may imagine two general techniques for searching for new particles. One of these is to look for a dramatic signal not expected from known physics, without specification of a model for the cause of the deviation being required. The other is to consider a given model, and to see what signatures it predicts that are inconsistent with known physics. Because of the subtlety of the signature involved a search for gluinos and squarks falls of necessity into the latter class.

3.1 Squark and Gluino Event Signature

The cascade decay of gluinos and squarks can produce, in the final state, a large number of quarks and gluons. Their pair production always produces a pair of LSPs. Thus squarks and gluinos are seen in the detector as jets produced by the quarks and gluons and as an imbalance of the transverse energy distribution, called missing transverse energy ($\not{E}_T$), caused by the non-

measurement of the LSPs. Thus a signal for which one may look is multiple jets and $\not{E}_T$.

3.2 Triggering

The data used in this analysis were collected during the August 1992—May 1993 run of the Tevatron (Run IA); this was the inaugural run of the DØ detector.

Several triggers were used to collect the data for this analysis. Each trigger required some combination of $\not{E}_T$ and jets, and during the course of the run, each was implemented with several different thresholds. We label the trigger MISSING_ET if there is no Level 2 jet requirement, and JET_MISS if there is a Level 2 jet requirement. The complete specification of these triggers, and the corrected integrated luminosity collected by each, is given in Table 3.1. The luminosity corrections are explained in sections 5.1.1 and 5.1.2. The codes used for describing the Level 1 trigger specifications are the following:

- **JT**(n, x) Requires at least n trigger towers with $E_T \geq x$ GeV,
- **MS**(x) Requires $\not{E}_T \geq x$ GeV,

and for Level 2:

- **L2J**(n, x, r) Requires at least n jets with $E_T \geq x$ GeV, using a cone jet algorithm with radius r,
- **L2MS**(x, s) Requires $\not{E}_T \geq x$ GeV and $\not{E}_T$ significance $\geq s$.

Config. name	MISSING_ET specification	JET_MISS specification	$\int \mathcal{L}\, dt$ (pb^{-1})
A	JT(1,3) + MS(35) L2MS(40,0)	JT(1,7) + MS(20) L2J(1,30,0.3) + L2MS(20,5)	0.148
A2	JT(1,3) + MS(35) L2MS(40,0)	–	0.045
B	JT(1,3) + MS(30) L2MS(40,0)	JT(1,7) + MS(20) L2J(1,30,0.3) + L2MS(20,5)	0.057
B2	JT(1,3) + MS(30) L2MS(40,0)	–	0.994
C	JT(1,3) + MS(30) L2MS(40,0)	JT(1,7) + MS(20) L2J(1,30,0.3) + L2MS(25,0)	0.824
D	JT(1,3) + MS(30) L2MS(35,0)	JT(1,7) + MS(20) L2J(1,20,0.5) + L2MS(25,0)	1.177
D2	JT(1,3) + MS(30) L2MS(35,0)	–	0.345
E	JT(1,3) + MS(30) L2MS(35,0)	JT(3,5) + MS(20) L2J(3,20,0.5) + L2MS(25,0)	4.143

Table 3.1: The trigger configurations used in this analysis and their associated integrated luminosities.

The $\not{E}_T$ significance is defined as the ratio of the $\not{E}_T$ for the event divided by the estimate of the $\not{E}_T$ resolution for the event, as determined from the total scalar E_T of the event [25].

3.3 Data Processing

In the DØ online cluster, data is written to two *online streams*; these data streams are written to different series of tapes, to allow faster handling of a small subset of the whole event sample. These streams are the *Express* (EXP) stream and the *All* (ALL) stream. The EXP stream comprises a select set of triggers, and represents about one tenth of the full data sample. The ALL stream, as the name indicates, includes all the events taken including those sent to the EXP stream. The triggers used for this analysis were not included in the EXP stream.

3.3.1 Event Reconstruction

The online streams consist of event in the raw data format. This format contains digitized values that describe the response of the individual detector elements rather than the physical quantities, such as particle momenta, we wish to measure. A complex FORTRAN program, DØRECO, is used to translate the raw data into such things as calorimeter energy deposits or hit locations on wires, and then to analyze these to produce physics objects such as jets, electrons, muons, and $\not{E}_T$. The reconstruction of jets and $\not{E}_T$ are described in detail in Chapter 4.

The ALL stream events were reconstructed on a farm of Silicon Graphics computers. In this analysis, we use the results of DØRECO v10, the first version to be used on the complete Run IA data sample. Because of the large number of events (13 million in Run IA) and because of the large size (about 20 kilobytes) of even our 'small' format Data Summary Tape (DST) events, it was not possible to store all the Run IA events on disk. Therefore, after reconstruction, the events were further filtered and segregated into *offline* streams. The RGE stream, which consisted of events passing one or more of a large array of offline filters, was stored on disk on the DØ file server cluster. One of the filters which contributed to this sample (called the SQGL filter) was constructed specifically for the collection of gluino and squark signal events. Later developments in the run made the retention of the complete RGE sample impractical; a further filtering and streaming of the events was then done. One of the filters used in this process (the SSY filter) was constructed for the retention of gluino and squark events.

3.3.2 Filtering

The SQGL and SSY filters were designed to keep the efficiency for the gluino and squark signal as high as possible, while reducing the rate to acceptable levels. To this aim, each filter was designed both to require a 'softened' version of the signal characteristics and to reject a major source of background.

The main background sources rejected by the SQGL and SSY filters were noise due to discharges in the calorimeter cells and energy deposits from par-

ticles associated with the Main Ring, which passes through the outermost (Coarse Hadronic) layer of the calorimeter. Both of these sources can produce 'jets' which are not associated with particles from an interaction. Although rare when compared to the rate of production of real jets, such jets produce $\not\!\!E_T$ in direct proportion to their E_T. Thus the $\not\!\!E_T$ trigger sample is highly enriched in such events.

To reject these events, the most basic technique used took advantage of the segmentation of the DØ calorimeter by considering the longitudinal profile of each jet. We considered the fraction of the total jet E_T which was contained in the electromagnetic calorimeter; this fraction is call the *electromagnetic fraction*, or EMF, of the jet. Jets with very high or very low EMF are suspect. Rejection based upon the EMF of the jets has a second beneficial effect. Since electrons are seen in the DØ calorimeter as highly electromagnetic jets, the rejection of events with such jets is also an extremely efficient method of rejecting electrons, such as those present in the decay $W \rightarrow e\bar{\nu}$, one of the significant backgrounds to a search based on $\not\!\!E_T$. To enhance the rejection of QCD events with $\not\!\!E_T$ due to mismeasured jets, we also rejected events in which a jet was found to be nearly back-to-back in azimuth with the direction of the $\not\!\!E_T$. And finally, we rejected events containing an electromagnetic cluster that passed a loose electron shape cut. The details of the cuts in the SQGL and SSY filter are listed below.

The SQGL filter required

- $\not\!\!E_T > 25$ GeV,

- leading E_T jet must have EMF > 0.05,

and the SSY filter required

- $\not{E}_T \geq 25$ GeV,
- at least 3 jets with $E_T \geq 15$ GeV,
- 3 highest E_T jets must satisfy $0.05 <$ EMF < 0.90 and $|\eta| < 3.5$.

Furthermore, the SSY filter *rejected* any event with one or more of the following:

- a jet with E_T (uncorrected) > 15 GeV and $|\eta| \leq 3.5$ and EMF < 0.05;
- any of the 3 leading E_T jets with $|\delta\varphi_k - \pi| < \pi/64$;
- $\sqrt{(\delta\varphi_1 - \pi)^2 + (\delta\varphi_2)^2} < 0.25$
- an electron or photon candidate with $E_T > 20$ GeV and $\chi^2 < 200$.

where we define $\delta\varphi_k$ as the azimuthal angle between $\vec{\not{E}}_T$ and the jet k, with the jets labelled in order of decreasing E_T. The quantity χ^2 is determined using a covariance matrix technique [26, 27]. For electrons with $E_T > 25$ GeV the efficiency of the χ^2 cut has been measured as greater than 95% [28].

Runs in which one of the detector subsystems was known to have malfunctioned were excluded from this analysis. There was a total of 9625 MISSING_ET and JET_MISS triggers in the SSY event sample.

Chapter 4

Jet and $\not{E}_T$ Reconstruction and Corrections

4.1 Reconstruction

The DØRECO program is the work of scores of physicists and many thousands of hours; it is too complex to describe in full detail here. Nevertheless, the overwhelming importance of jet and $\not{E}_T$ measurements to this analysis warrant a detailed description of these aspects of the reconstruction.

4.1.1 Jet Reconstruction

A quark or gluon produced at high transverse momentum reveals itself in the detector as a collimated beam or *jet* of hadrons. The exact prescription by which one constructs jets clearly affects what number of jets is detected, as well as their kinematic features.

In DØ jets are identified by the calorimeter. Loosely speaking, a jet is seen as a localized cluster of energy deposits. A more specific definition is necessary for quantitative analysis.

We define the directed energy vector $\vec{E}_i$ associated with a calorimeter cell i as

$$\vec{E}_i = \hat{n} E_i, \tag{4.1}$$

where $\hat{n}$ is the unit vector pointing from the interaction point to the center of cell i, and E_i is the magnitude of the energy deposit in cell i. The quantity $\vec{E}_k^{\text{Tower}}$ is the energy vector associated with projective tower k; it is the vector sum over all cells in tower k of the cells' energy vectors. The transverse energy of the tower is the magnitude of the projection of this vector into the transverse plane. Thus we define

$$E_T^{\text{Tower}} = \sqrt{(E_x^{\text{Tower}})^2 + (E_y^{\text{Tower}})^2}. \tag{4.2}$$

Jet finding in DØ starts from these tower E_T values.

In $p\bar{p}$ physics the standard definition of a jet has used a fixed cone algorithm [29]. This algorithm uses a cone of fixed radius R in $\eta \times \varphi$. In DØ this algorithm is implemented as a three step process: preclustering, cone clustering, and splitting/merging.

Preclustering Preclustering begins with an E_T ordered list of calorimeter towers. The highest E_T tower is taken as a precluster *seed*. With it are associated all adjacent towers with $E_T \geq 1$ GeV. These neighbors are then checked for further neighbors with $E_T \geq 1$ GeV, and any found are added to the precluster. This continues to a maximum extent of a square 'ring' including all towers within ± 0.3 units in η or φ. The towers included in the precluster are removed from the seed list, and the

remaining tower with the greatest E_T is used as the next seed. This continues until no seed with $E_T \geq 1$ GeV remains on the list. At this point all towers with $E_T \geq 1$ GeV have been assigned to a cluster.

Cone clustering Cone clustering begins with the preclusters found in the previous stage. Starting with the highest E_T precluster, the E_T weighted (η, φ) centroid of the precluster is found and identified as the jet axis. All towers within a radius of R (in this analysis we use $R = 0.5$) in $\eta \times \varphi$ are assigned to the jet. The jet axis is recalculated using these towers, and the process is iterated until the jet axis moves a distance less than 0.001 in $\eta \times \varphi$ space between iterations. A maximum of 50 iterations is allowed to prevent the rare case of a bistable solution from using an unreasonable amount of processing time. If the resulting jet has $E_T > 8$ GeV, it is stored, and splitting/merging (as described below) is attempted on the jet. The process is then begun on the next precluster.

Splitting/Merging The first jet by definition can share no energy with a previously found jet. Beginning with the second each new jet is checked to see if it shares any towers with a previously found jet. If one or more towers are shared, the jets axes are compared; if they are separated by a distance of less than 0.01 in $\eta \times \varphi$, the 'new' jet is merely a re-finding of the old jet. This can happen due to roundoff error in the calculations. In this case the 'new' jet is dropped. If they are not identical a decision on whether the system is one or two jets is necessary. To decide, we

determine the fraction $f_{\rm SM}$, defined by

$$f_{\rm SM} = \frac{E_T^{\rm shared}}{E_T^{\rm min}} \tag{4.3}$$

where $E_T^{\rm shared}$ is the sum of the transverse energies of the common towers, and $E_T^{\rm min}$ is the lesser of the transverse energies of the two jets clusters. If $f_{\rm SM} \leq 0.5$ then two jets are made and each contested cell (not tower) is assigned to the jet whose center is nearest that cell; otherwise, the system is a single jet and all the towers are assigned to it. In either case the jet axis is recalculated one last time, including all the appropriate towers; this is not iterated.

The final jets' kinematic quantities are defined by

$$E_i = \sum_{\text{cells } k} E_i^k, \tag{4.4}$$

$$E_T = \sum E_T^k, \tag{4.5}$$

$$E = \sum E^k, \tag{4.6}$$

$$\varphi = \arctan(E_y/E_x), \tag{4.7}$$

$$\vartheta = \arccos\left(E_z/\sqrt{E_x^2 + E_y^2 + E_z^2}\right), \tag{4.8}$$

$$\eta = -\ln\tan(\vartheta/2), \tag{4.9}$$

where E_i is the directed energy in cartesian direction $i = x, y, z$. Note that E_T is the sum of the individual tower transverse energies, not the magnitude of the vector components, and similarly E is the sum of the individual tower energies. Note also that η and θ are defined with respect to the interaction vertex which is not always at $z = 0$. When reference to a location in the detector is needed

we use detector η ($\eta_{\rm det}$) which is defined as the pseudorapidity as measured from $z = 0$.

4.1.2 $\not\!\!E_T$ Reconstruction

In DØ the calculation of $\not\!\!E_T$ is based upon energy deposits considered at the level of individual cells. With the cell energy vector $\vec{E}_i$ defined in Equation 4.1, the vector $\vec{\not\!\!E}_T$ is defined by

$$\begin{aligned} \not\!\!E_x &= -\sum_{\text{cells } i} E_{xi}, \\ \not\!\!E_y &= -\sum_{\text{cells } i} E_{yi}, \\ \vec{\not\!\!E}_T &= \begin{bmatrix} \not\!\!E_x \\ \\ \not\!\!E_y \end{bmatrix}. \end{aligned} \tag{4.10}$$

The sums are over all cells in the calorimeter. The missing transverse energy, $\not\!\!E_T$, is the magnitude of this vector; also useful is $\varphi_{\not\!\!E_T}$, the azimuthal direction of the $\not\!\!E_T$ vector, defined by

$$\varphi_{\not\!\!E_T} = \arctan(\not\!\!E_y / \not\!\!E_x). \tag{4.11}$$

The $\not\!\!E_T$ resolution of the DØ detector is studied in detail in references [25, 30].

We define the scalar E_T ($E_T^{\rm scalar}$) as the scalar sum over all calorimeter cells of the transverse energy:

$$E_T^{\rm scalar} = \sum_{\text{cells } i} E_{Ti}. \tag{4.12}$$

4.2 Corrections

No reconstruction program is perfect. During the course of the run, we were able to make improvements in the determination of jet energies, electron energies, and missing transverse energy calculations. While there were insufficient computing resources to allow reprocessing of all the data for each minor algorithmic improvement, it was possible to implement many of them after the fact, on the reconstructed DSTs. We are concerned here with two such corrections, specifically those for jets and for $\not\!\!E_T$.

4.2.1 Jet Corrections

The energy scale used in the DØRECO program was transferred from the testbeam, where it was measured for single pions [21]. The testbeam, however, consisted of single pions of known energy, not jets of many particles. Furthermore, many of the particles in even a high energy jet are of low energy, and nonlinearity in the calorimeter's energy response makes corrections to the reconstructed jet energy necessary if one wishes to recover the energy of all the particles contained within the jet cone.

In this analysis we used DØ's standard jet correction algorithm. This algorithm corrects the jet energy, E_T, EMF and direction as a function of energy, η and EMF of the jet. Furthermore, it *removes* any isolated electron or photon candidate from the jet before correction; such electromagnetic objects are corrected separately and added back in for the final result.

The correction may be thought of in four parts. The first part corrects

for the EMF dependence of jet response, the second corrects for the proper energy scale in the central region ($|\eta| \leq 0.7$), the third transfers the correction to the forward region($|\eta| > 0.7$), and the fourth removes contributions from the underlying event and uranium noise. Separate from these is the determination of what ought to be corrected as a jet, and what should be treated as an electron or photon.

Determining Jet Corrections

As a prelude to actual jet corrections, the energy scale of the entire electromagnetic calorimeter was set by making the DØ sample of $Z \rightarrow e\bar{e}$ decays produce a mass peak at the value measured by the LEP experiments. This required about a +2% correction to the energy scale transferred from the test-beam for the forward calorimeters, and about +7% correction in the central calorimeter.

EMF Dependence. To determine the EMF dependence of the jet we used a sample of dijet events. We define the ratio R_{EMF} as

$$R_{\mathrm{EMF}} = \frac{E_T^{\mathrm{A}}}{E_T^{\mathrm{B}}} \tag{4.13}$$

where E_T^{A} is the measured transverse energy of the 'probe' jet and E_T^{B} is that of the 'trigger' jet, which was required to trigger the event. We binned the events in terms of ε_A, the EMF of the probe jet, and calculated for each ε_A the mean value of R_{EMF} , thus averaging over other variables on which the jet response may vary (such as ε_B). Only if there is an EMF dependence on the

response shall R_{EMF} vary as a function of ε_A, and consequently the variation of R_{EMF} with ε_A is, up to a factor, the EMF dependence of the jet response.

Central Jet Scale. To determine the jet energy scale for the central region we used a Missing Transverse Energy Projection Fraction (MPF) technique, similar (but not identical) to that pioneered by CDF [31]. In DØ this was implemented using a set of events containing a 'photon' and one or more jets. The 'photon' was defined as an electromagnetic cluster (EMF ≥ 0.90) with no associated track and thus the sample contains both direct photons and isolated π^0 decays; what is relevant for the method to work is that both particles' energy scale is set by that of the electromagnetic calorimeter. In order to remove those $W \to e\bar{\nu}$ events in which the electron track was lost, and also to remove noise events, those events in which the component of $\vec{\not{E}}_T$ in the direction of the photon or leading jet was large (compared to the E_T of the photon or leading jet E_T, respectively, were eliminated. We define

$$\mathrm{MPF} = \frac{-\hat{n} \cdot \vec{\not{E}}_T}{E_T^\gamma} \tag{4.14}$$

where $\hat{n}$ is the unit vector defined by the direction of the photon, E_T^γ is the corrected transverse energy of the photon, and $\vec{\not{E}}_T$ is the measured (vector) missing transverse energy of the event. This quantity was measured as a function of $E_T^\gamma \cosh(\eta_{\mathrm{jet}})$ over the range $E_T^\gamma \cosh(\eta_{\mathrm{jet}}) = 5 \ldots 100$ GeV, in 5 GeV bins.

These events may have nonzero measured $\not{E}_T$ for two reasons:

1. the measurement fluctuations inherent in sampling calorimetry;

2. a systematic difference between the electromagnetic energy scale and the energy for jets.

In a large sample of events, the $\vec{\not{E}}_T$ caused by (1) shall not be correlated with the direction of the photon, while $\vec{\not{E}}_T$ caused by (2) shall either be correlated or anti-correlated, depending on the ratio of the energy scales.

While this gave the correction factor for each value of $E_T^\gamma \cosh(\eta_{\rm jet})$, what is needed is a correction for each measured jet. In a purely 1 photon + 1 jet final state, the true jet energy is given by $E_{\rm jet} = E_T^\gamma \cosh(\eta_{\rm jet})$. For each $E_T^\gamma \cosh(\eta_{\rm jet})$ bin, the mean value of $E_{\rm jet}$ was determined; it is to jets of this energy that we apply the correction corresponding to $\mathrm{MPF}(E_T^\gamma \cosh(\eta_{\rm jet}))$. Linear interpolation is used for values of $E_{\rm jet}$ between bin centers. The central region energy scale factor $R_{\rm jet}$ is then

$$R_{\rm jet} = 1 - \mathrm{MPF}(E')\,, \tag{4.15}$$

where E' is the value of $E_T^\gamma \cosh(\eta_{\rm jet})$ associated with the energy of the jet which we are correcting.

η-Dependent Jet Scale. To determine the η dependence of the jet scale we used a sample of dijet events with one 'trigger' jet, which was required both to be central ($|\eta| \leq 0.7$) and to have triggered the event, and one 'probe' jet which was allowed to be at any value of η. Two versions of the forward jet correction were produced. For the first we used dijet balancing and for the second we used an MPF technique similar to that described above, but using the central jet in place of the photon.

The dijet balance analysis yielded the correction used for determining the energy and E_T of forward jets. This method was chosen because the correction it produces accounts not only for an η dependent energy scale but also for the energy that leaks out of the cone of a forward jet, which is much greater than the leakage for centrals jets. The smaller physical size of the 0.1×0.1 towers in the forward region causes the greater leakage.

The MPF method yielded the appropriate jet correction when such out-of-cone correction is not wanted, as is the case for the $\not{E}_T$ correction discussed in Section 4.2.2 below.

Underlying Event and Noise Correction. The correction for underlying event energy and uranium noise energy were determined as a function of cone size and η. The underlying event energy in a jet cone of radius R at given η was determined from a study of minimum bias triggers. The energy in the cone due to uranium noise was estimated by considering data taken without zero suppression, and is independent of η.

Application of Jet Corrections

The jet correction algorithm is coded in the routine QCD_JET_CORRECTION, which applies all the corrections detailed above. One more complication exists: to what objects ought the jet correction be applied? Because electrons and photons form energy clusters in the calorimeter they are identified by the jet finder as jets. The specification of electromagnetic (electron or photon) or hadronic jets is made after the fact. Because the jet finding algorithm does

not give the best measure of the energy of electrons or photons, use of the jet corrections on them is inappropriate.

To identify those jets that ought to be corrected as electrons or photons, an isolation requirement is placed on electron/photon candidates found by the electron/photon finding algorithm. (This algorithm performs nearest neighbor clustering using only the electromagnetic calorimeter and the first layer of the hadronic calorimeter). We define an isolation fraction $f_{\rm ISO}$ as

$$f_{\rm ISO} = \frac{E^{0.4} - E^{0.2}_{\rm EM}}{E^{0.2}_{\rm EM}}; \tag{4.16}$$

where $E^{0.4}$ is the energy in a cone of radius 0.4 about the EM cluster axis, including energy in the EM calorimeter and the first layer of the hadronic calorimeter, and $E^{0.2}_{\rm EM}$ is the energy in a cone of radius 0.2 about the EM cluster axis, including only energy in the EM calorimeter. An electron or photon candidate with $f_{\rm ISO} \leq 0.15$ is considered isolated. Isolated EM objects are subtracted from the associated jet (the association is done by identifying the jet that contains the specific cells included in the EM object); the subtraction is done on individual components of the directed energy vector, and on the E_T and energy of the jet as well. If the remaining jet 'stub', after subtraction, falls below the 8 GeV threshold used by the jet finder, it is dropped; if more than 8 GeV remains (as is possible for the case of an EM cluster at the edge of a jet cone) it is corrected as a jet, after recalculation of the jet η and EMF to reflect the excision of the EM object. The subtracted EM cluster is corrected by the EM energy scale, and is then added back to the corrected jet 'stub'; the η and EMF are again recalculated, and the result is the final corrected jet.

Figure 4.1 shows the EMF dependence of the jet correction for jets at fixed η and E_T; Figure 4.2 shows its dependence on η for fixed EMF and E_T; Figures 4.3 and 4.4 show the dependence on E_T for fixed EMF and at two different values of η. Figure 4.5 shows the measured jet resolution in the central, ICD, and forward regions.

4.2.2 $\not\!\!E_T$ Corrections

In the determination of the correction for jets it was possible to use a set of events (the photon + jet(s) sample) in which the true energy of the jet could be determined. There is, unfortunately, no equivalent sample of events with well-definable nonzero $\not\!\!E_T$. Indeed, $\not\!\!E_T$ is not the measurement of a positive detector response to the particle of interest (neutrino or LSP) but rather it is a quantity inferred from the detector response to all *other* parts of the event. The corrections to $\not\!\!E_T$ are thus not determined by the $\not\!\!E_T$ itself, but rather by what else is present in the event.

The $\not\!\!E_T$ correction algorithm uses three separate corrections: that for electron and photons, that for jets, and a 'soft recoil' correction. Only the soft recoil correction, described below, is unique to the $\not\!\!E_T$ correction. The correction is performed in three steps: removal of uncorrected objects, correction of the soft recoil, and replacement of corrected objects.

Remove Uncorrected Objects We remove the uncorrected isolated electrons and photons, and jets (some of which have had isolated electrons and photons excised), from the $\not\!\!E_T$ by adding the vector sum of the found

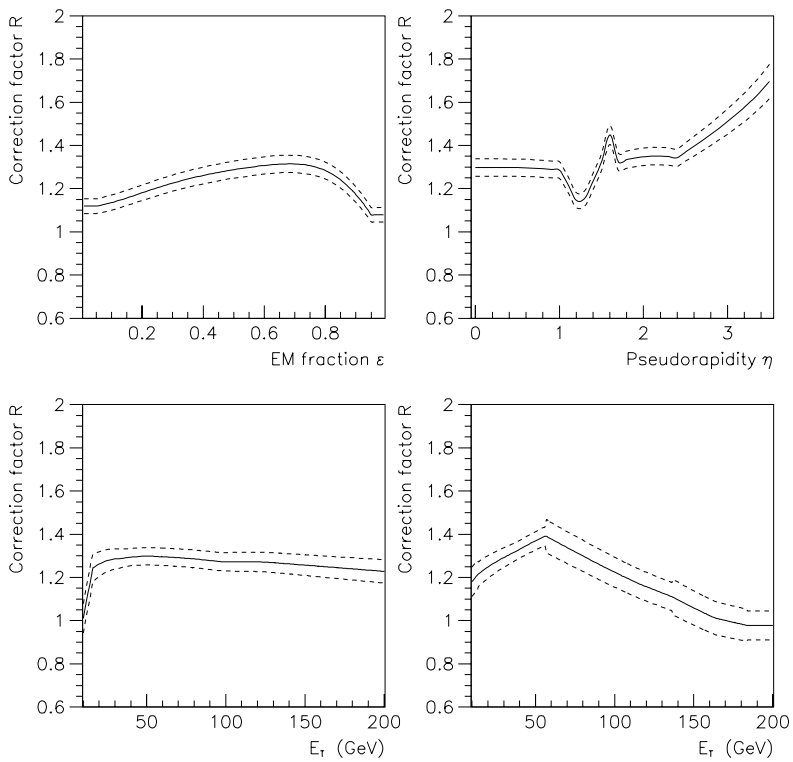

Figure 4.1: The EM fraction dependence of the $R = 0.5$ jet energy correction. This curve is for jets with $E_T = 50$ GeV and $\eta = 0.0$. For all these figures, the solid curve is the nominal correction and the dotted curves show the systematic error band.

Figure 4.2: The η dependence of the jet energy correction. This curve is for jets with $E_T = 50$ GeV and EMF $= 0.55$.

Figure 4.3: The E_T dependence of the jet energy correction for central jets. This curve is for jets with EMF $= 0.55$ and $\eta = 0.0$.

Figure 4.4: The E_T dependence of the jet energy correction for forward jets. This curve is for jets with EMF $= 0.55$ and $\eta = 2.5$.

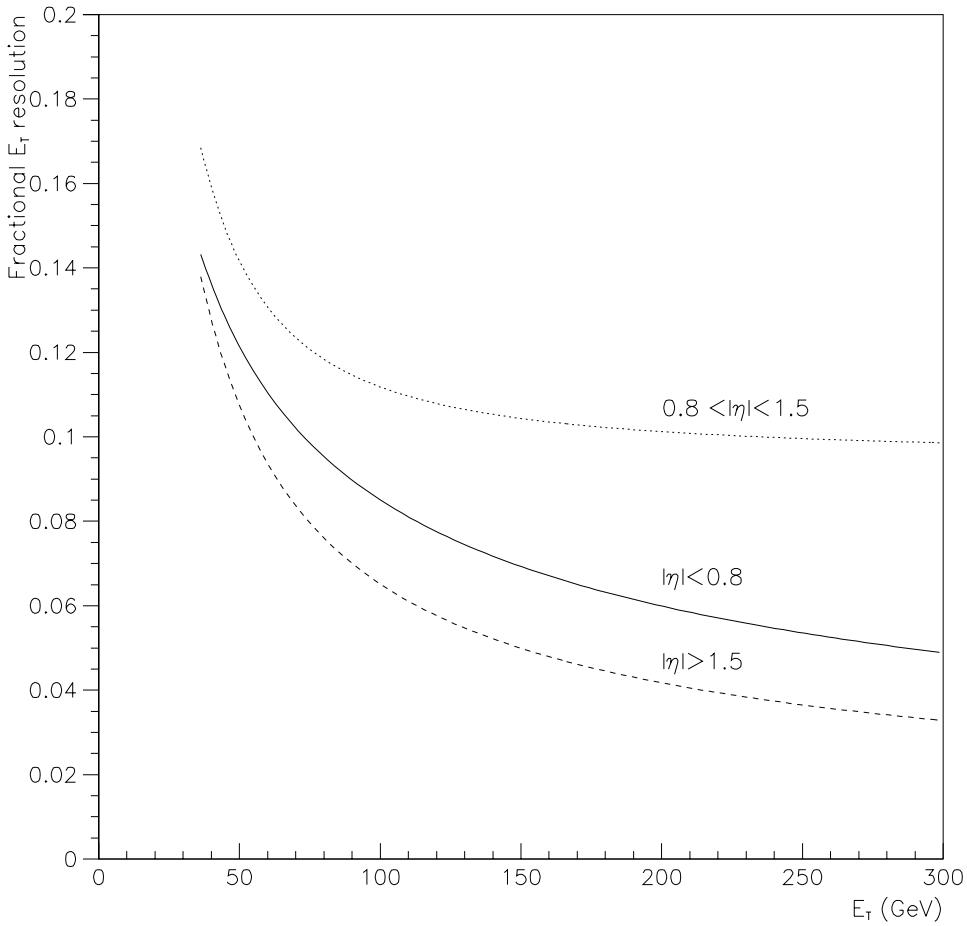

Figure 4.5: The fractional jet E_T resolution σ_{E_T}/E_T as a function of E_T for different rapidity regions. The dotted line is for the intercryostat region, the solid line for the central region, and the dashed line for the forward region.

objects' E_x and E_y to the $\not{E}_T$ components $\not{E}_x$ and $\not{E}_y$.

Correct Soft Recoil The remaining unclustered energy deposits, called the *soft recoil*, is scaled by a factor determined from a study of $Z \rightarrow e\bar{e}$ events with no jets. This scaling function was determined by requiring that the unclustered energy in the Z event balance exactly the momentum of the Z, which was defined by scaling the energy of the electrons to produce exactly the LEP value of the Z mass.

Replace Corrected Objects The isolated electrons and photons are corrected and then added back into the $\not{E}_x$ and $\not{E}_y$ components. The jets are also corrected, but this time the underlying event and uranium noise corrections, as well as the out-of-cone correction, are not done, so that such energy is not missing only from the jet cone (in the case of the underlying event and uranium noise) or is not double-counted (in the case of the out-of-cone correction); recall our earlier definition (Equation 4.10) of $\not{E}_T$ includes all cells in the calorimeter, not just those in jet cones.

Chapter 5

Analysis

Analysis of a data sample for evidence of new physics takes place in three steps: reduction of the data sample, estimation of expected number of background events, and estimation of the signal expected from a model of the new physics for which one is searching. The standard technique physicists use to filter a data sample is the introduction of requirements, called *cuts*; only those data that satisfy these requirements are carried over to the next step in the analysis. There is a measure of artistry involved in this process. The art lies in choosing those quantities and cuts which retain the greatest amount of signal while rejecting the greatest amount of background. In this chapter we describe the data reduction and background estimate for our squark and gluino search.

5.1 Signal Selection Cuts

The primary signal selection criterion we imposed was the requirement of large $\not{E}_T$ and three or more jets. Since there are several Standard Model

processes that may produce such a final state we also employed several cuts designed to reduce their presence. Additionally, we introduced several cuts to reduce detector-induced backgrounds.

Signal selection started with the SSY stream described in 3.3.2. Recall that the SSY stream was selected on the basis of uncorrected quantities. The corrections described in Chapter 4 were applied to these events before any of the cuts described in this chapter were applied. In this section we describe in detail each of the cuts applied to the corrected events.

5.1.1 Single Interaction Cut

The most important cut in this analysis was the requirement of large $\not\!\!E_T$. Reconstruction of $\not\!\!E_T$ requires measurement of the z position of the primary interaction vertex. Because of the high instantaneous luminosity reached by the Tevatron during the 1992–1993 run, many of the events collected contained more than one interaction; in these events correct identification of the *primary* interaction vertex is difficult. For this analysis such events were rejected.

We used an algorithm called the MULTIPLE_INTERACTION_TOOL (MITOOL) to implement the single interaction requirement [32]. The MITOOL combines information from several sources to identify an event as a single or multiple interaction. The number of vertices found by the tracking chambers and collision timing from the LØ system are both considered. The efficiency of the MITOOL is studied in reference [33]; to understand its efficiency a digression on the subject of multiple interactions is in order.

An event which fires a trigger must contain at least one hard scattering. Because the hard scattering cross section is a miniscule fraction of the total inelastic cross section, the probability for a trigger to contain two hard scatterings is negligible. We are concerned, however, with the probability of encountering one or more soft inelastic interactions overlapping with the hard scattering on which we triggered.

The expectation value $\bar{n}$ of the number of interactions per beam crossing depends on the instantaneous luminosity $\mathcal{L}$, the total inelastic cross section σ to which the LØ trigger is sensitive (called the *minimum bias* cross section), and the time τ between crossings, according to

$$\bar{n} = \mathcal{L}\sigma\tau. \tag{5.1}$$

In DØ we have $\sigma\tau = 0.151 \cdot 10^{-30}$ cm^2 s [34].

The probability $P(m)$ for a given crossing to contain m minimum bias interactions is given by the Poisson distribution with mean $\bar{n}$,

$$P(m) = \frac{\bar{n}^m e^{-\bar{n}}}{m!}. \tag{5.2}$$

A *single* interaction is a hard scattering coincident with zero minimum bias collisions and occurs with a probability $P(0) = e^{-\bar{n}}$ for each triggered event. A *multiple* interaction is a hard scattering coincident with one or more minimum bias collisions and occurs with a probability $P(1^+) = \sum_{m=1}^{\infty} P(m) = 1 - P(0) = 1 - e^{\bar{n}}$ for each triggered event. We shall return to these equations shortly.

Figure 5.1 shows the fraction f_1 of events identified by the MITOOL as single interactions as a function of the instantaneous luminosity of the run. We

may adequately describe these data with a theory that assigns an efficiency ε with which the MITOOL identifies a true single interaction correctly, and a mistake rate r which is the probability with which the tool mistakes a multiple interaction for a single interaction. We then have

$$\begin{aligned} f_1 &= \varepsilon P(0) + r P(1^+) \\ &= \varepsilon e^{-\bar{n}} + r\left(1 - e^{-\bar{n}}\right) \end{aligned} \tag{5.3}$$

with $\bar{n}$ dependent on the instantaneous luminosity $\mathcal{L}$ according to Equation 5.1. The solid line shows a minimum-χ^2 fit to the form

$$f_1 = \varepsilon e^{-\alpha\mathcal{L}} + r\left(1 - e^{-\alpha\mathcal{L}}\right). \tag{5.4}$$

The data have negligible statistical errors; the error bars on the points are systematic error bars scaled to produce a χ^2 per degree of freedom of unity. The fitted parameters are

$$\begin{aligned} \alpha &= (0.15 \pm 0.04) \cdot 10^{-30}\ \mathrm{cm}^2\ \mathrm{s} \\ \varepsilon &= 92 \pm 4\% \\ r &= 6^{+12}_{-6}\% \end{aligned}$$

The value of α agrees well with the expected value of $\sigma\tau$ given above.

Our use of the MITOOL to select single interaction events made it necessary to correct the integrated luminosity for each run to extract the equivalent luminosity for single interactions. This was done using the averaged instantaneous luminosity of each run. The correction includes the 92% efficiency of the MITOOL and also adds 6% of the equivalent multiple interaction luminosity

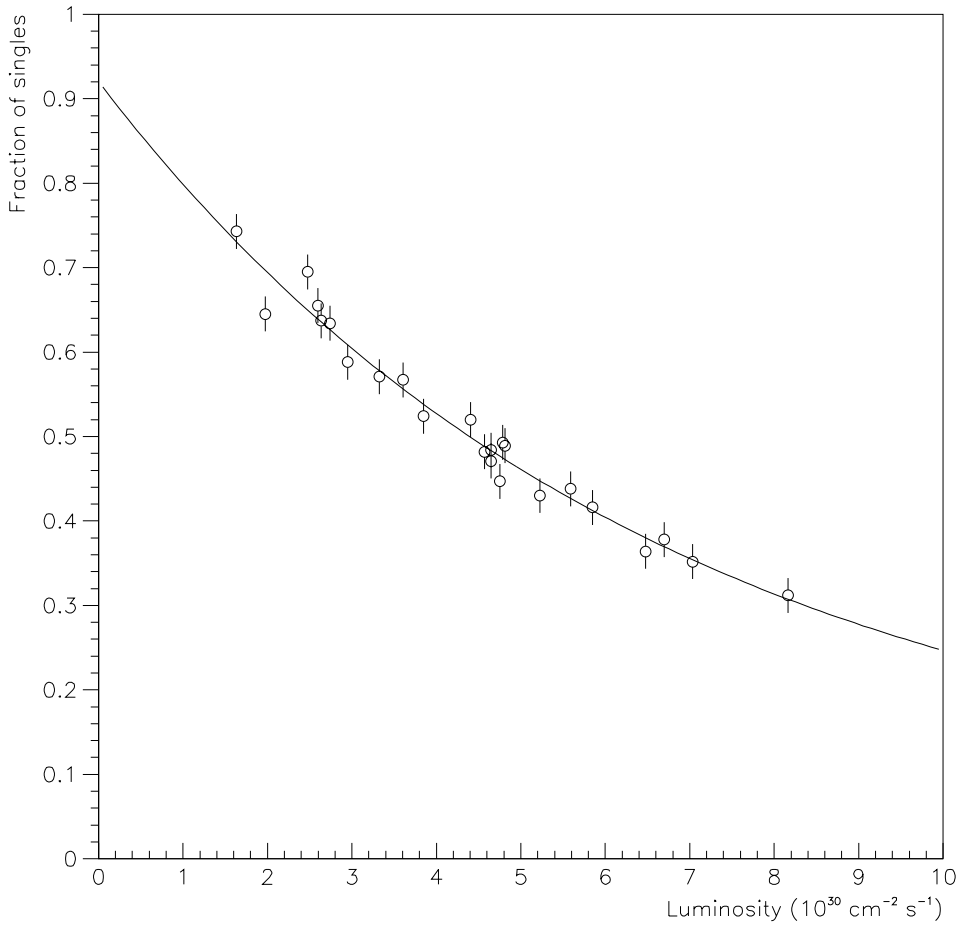

Figure 5.1: The fraction of events identified by the MITOOL as single interactions as a function of the instantaneous luminosity. The line is the fit described in the text.

as dictated by the mistake rate of the MITOOL. These luminosities are listed in Table 3.1, page 44. The total luminosity corrected for use of the MITOOL was 7.7 ± 1.0 pb^{-1} ; the error includes the errors in the efficiency and mistake rate of the MITOOL and a 12% systematic error in the luminosity reported by the DØ luminosity monitors, added in quadrature.

Since the MITOOL does not have perfect efficiency there shall be some contamination of our sample by multiple interaction events. Misidentified multiple interactions fall into two classes:

1. those in which the minimum bias collision produces so few tracks and deposits so little energy that it is unnoticed;

2. those in which the minimum bias collision occurs so close in z to the hard scattering that no second vertex is resolved (≈ 2 cm).

Mistakes of the MITOOL could be dangerous if they allow background events to masquerade as signal, or if they cause us to miss signal events. We have already included the efficiency of the tool in the calculation of our corrected luminosity. We now consider how our signal of $\not{E}_T$ and three or more jets can be faked by these failures.

In events of the first kind the minimum bias collision by definition has little influence. In events of the second kind the $\not{E}_T$ reconstruction is not sensitive to a few centimeters' movement of the vertex z location. Furthermore, the inclusive cross section for jets with $E_T > 25$ GeV is more than a factor of 1000 smaller than the minimum bias cross section ($\approx 30\,\mu$b compared to 43 mb)[35],

so the influence of these events is merely the increase in luminosity reflected by the factor r in Equation 5.3.

In addition to the use of the MITOOL we placed a requirement that the scalar E_T be positive and less than the full available cms energy of the collision, 1.8 TeV. This cut is of course fully efficient for single interactions; we used it to remove a few events contaminated by particles from the Main Ring, and one clear detector electronics failure.

A total of 3811 events passed the single interaction requirement.

5.1.2 Vertex z Cut

In order to assure that the event is well contained in the calorimeter we required that the z location of the interaction vertex satisfy -80 cm $< z <$ 60 cm. The asymmetric interval was used because the beam crossing point (the center of the vertex z distribution) was located near $z = -10$ cm during Run IA. The vertex z distribution was well described by a Gaussian with mean -10 cm and width 30 cm; this gives an efficiency of 95% for this cut. The integrated luminosity corrected for this cut is 7.4 ± 1.0 pb^{-1} .

A total of 3730 events passed this cut.

5.1.3 $\not\!\!E_T$ Cut

We chose a high $\not\!\!E_T$ requirement to ensure full efficiency of our trigger and earlier filtering and to drastically reduce the backgrounds while keeping substantial signal efficiency. We retained those events with $\not\!\!E_T \geq 75$ GeV.

Figure 5.2 is a histogram of the $\not{E}_T$ spectrum of these events. Figure 5.3 is a histogram of the *uncorrected* $\not{E}_T$ of these same events; note the sharp cutoff near 50 GeV, which indicates that our earlier cut on uncorrected $\not{E}_T$ at 25 GeV produces no loss of events in the final sample.

A total of 107 events passed the $\not{E}_T$ cut.

5.1.4 Three Jet Cut

The number of jets found in an event is dictated by the algorithm and E_T threshold used to define a jet. For this analysis a low E_T threshold is attractive because of the soft jet E_T spectrum of the squark and gluino production signal. Too low a threshold is impractical because of decreasing reconstruction efficiency and increasing uncertainty in the jet corrections. We chose a requirement of three or more good jets above a threshold of 25 GeV.

For the purposes of this analysis, a *good* jet was defined as one which satisfied several quality criteria. Most of these cuts were selected to reject jets formed by *noise*, that is, signals from the calorimeter not associated with energy deposited by particles from the interaction. Although the rate of production of noise jets is small in comparison to the rate of production of real jets in the E_T range of interest (a typical rate for a low E_T jet trigger due to noise is 1 per second; the rate due to real jets at an instantaneous of 5×10^{30} cm^{-2} s^{-1} is several thousand per second), the $\not{E}_T$ event sample is highly enriched in such events.

First, we required $0.10 < \text{EMF} < 0.90$. This cut removed most 'jets'

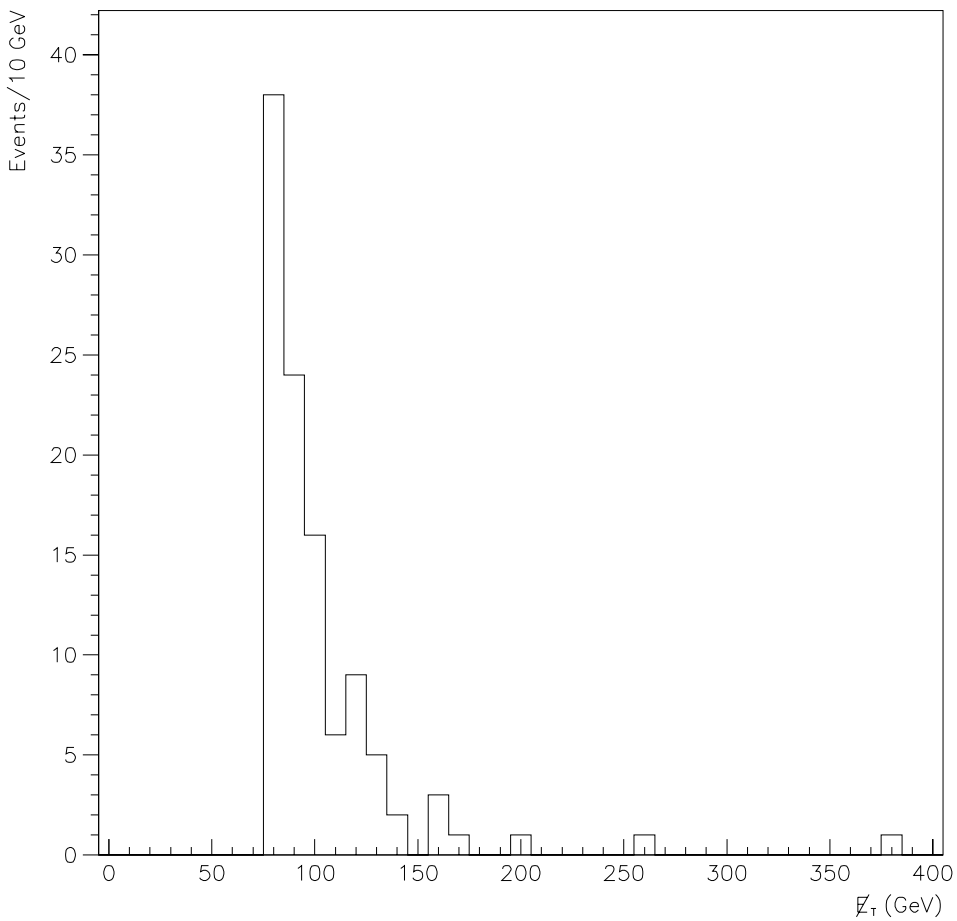

Figure 5.2: The $\not{E}_T$ distribution of the 107 events passing the cut $\not{E}_T \geq 75$ GeV.

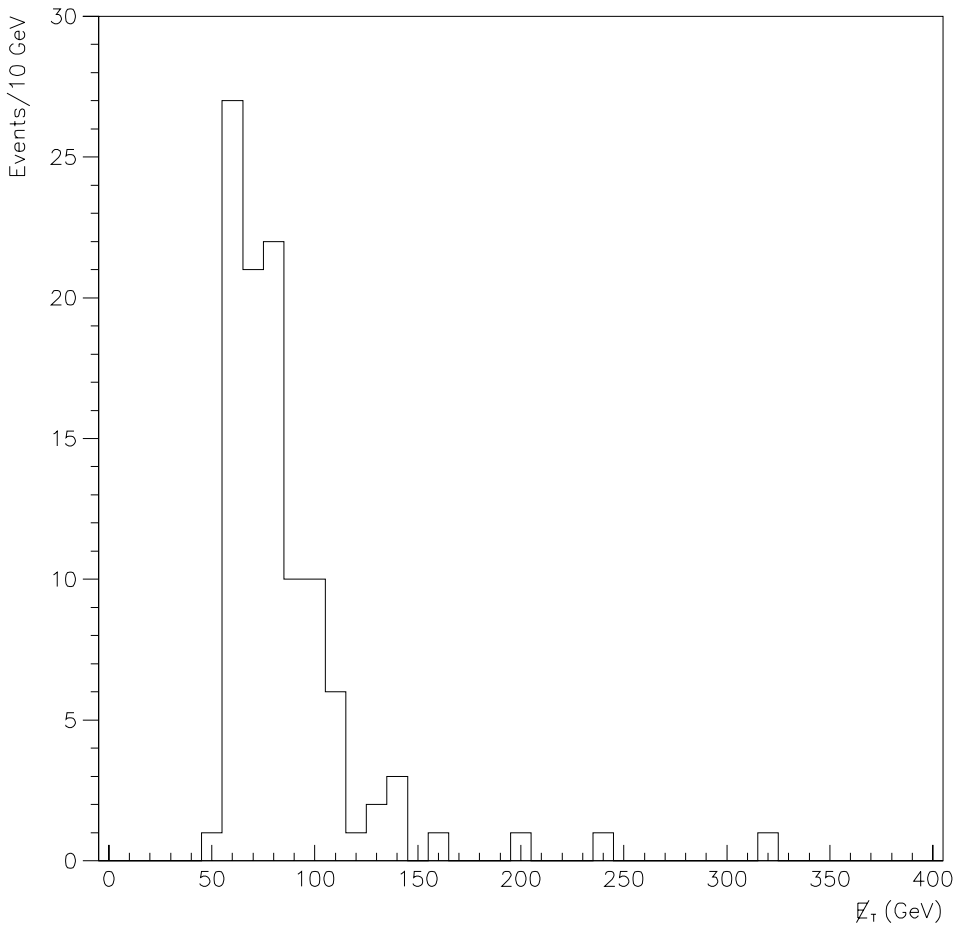

Figure 5.3: The uncorrected $\not{E}_T$ distribution of the 107 events passing the cut on corrected $\not{E}_T \geq 75$ GeV.

which are formed around noisy cells. This cut was also used to assure that the jet was a *hadronic* jet, that is one produced by a quark or gluon in the partonic final state. Recall that the DØ jet finder has no hadronic requirement, and that isolated high E_T electrons and photons in the final state are found as jets by this algorithm. Second, we required that less than 40% of the jet E_T be deposited in the coarse hadronic (CH) layer of the calorimeter. This removed jets caused by noise in the CH modules, and also removed jets induced by particles from the Main Ring bypass. Third, we required that the ratio of the energies of the two highest energy cells, $r = E_1/E_2$, be less than 10. This cut made the best use of the fine segmentation of the DØ calorimeter to reject jets formed around noisy cells. The efficiency of these cuts for retaining good jets is studied in [36] for the $r = 0.7$ cone algorithm, under a slightly different EMF cut. With the same analysis method used on the $r = 0.5$ cone algorithm, and with the cuts defined for this analysis, we find the efficiencies listed in Table 5.1 for jets in the central region [37]. Similar efficiencies are found for the intercryostat and forward regions.

A total of 47 events passed this cut.

5.1.5 ICR Cut

In the part of the intercryostat region (ICR) extending from $1.1 < |\eta_{\rm det}| < 1.4$ the coverage of the electromagnetic calorimeter is incomplete. The reason can be seen in Figure 2.7 on page 30: in this region particles from the interaction point pass through little of CCEM or ECEM, and much of the central

Jet E_T (GeV)	Efficiency (%)
8 – 15	94.7 ± 0.3
15 – 25	95.0 ± 0.3
25 – 40	95.1 ± 0.3
40 – 60	95.5 ± 0.3
60 – 80	95.4 ± 0.3
80 – 100	95.0 ± 0.3
100 – 130	94.6 ± 0.3
130 – 160	94.2 ± 0.4
160 – 200	93.9 ± 0.6
200 – 450	94.0 ± 0.8

Table 5.1: The cumulative efficiency for the jet quality cuts as a function of the jet E_T. The error is statistical plus systematic, added in quadrature.

and end cryostat walls. Electrons in this region are frequently not identified as electrons and, since the energy sampling in this region is small, their energy resolution is poor. These electrons contribute to poor $\not\!\!E_T$ measurement as well as masking $W \rightarrow e\bar{\nu}$ decays. To remove such events we rejected any event in which the highest E_T jet was in the region $1.1 < |\eta_{\rm det}| < 1.4$. Figure 5.4 shows the distribution of $\eta_{\rm det}$ for the 3730 events passing the vertex z cut in Section 5.1.2 above. The sharpness of the peak is consistent with being caused by electrons, which form narrow jets, and not hadrons which form broad jets.

A total of 45 events passed this cut.

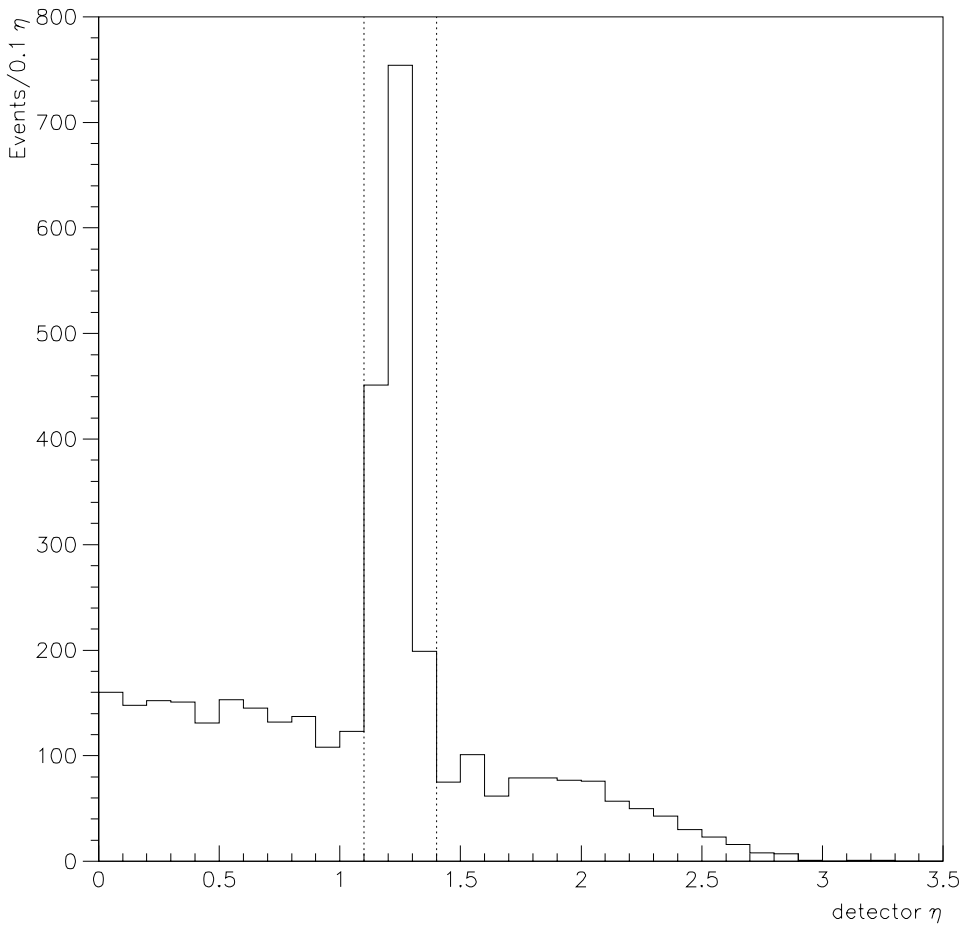

Figure 5.4: The detector η distribution of the leading jet for the 3730 events passing the vertex z cut. Events in which the leading jet fell into the region $1.1 < |\eta_{\rm det}| < 1.4$ (bounded by the dotted lines) were rejected.

5.1.6 Jet – $\not\!\!E_T$ Correlation Cut

It is possible for an event to contain nonzero measured $\not\!\!E_T$ caused solely by the imperfect jet resolution of the detector. In an event with perfectly measured jets the jets shall nearly balance in E_T; the imbalance due to fluctuations in the underlying event is very small compared to the values of $\not\!\!E_T$ with which we are concerned. If one or more of the jets is very poorly measured, falling into either the high or low tail of the jet resolution distribution, the jets shall not balance and the event shall have large measured $\not\!\!E_T$. In these cases we expect the azimuthal direction of the $\not\!\!E_T$ to be correlated with the direction of the poorly measured jet. If the measured jet energy is a fluctuation up, the $\not\!\!E_T$ opposes the jet; if the fluctuation is down, the $\not\!\!E_T$ aligns with the jet. The presence of other energy deposits with imperfect resolution tends to smear this correlation but not to eliminate it.

To remove such events from the sample we made cuts on the angular correlation between the jets and the $\not\!\!E_T$. We ordered the jets in terms of decreasing E_T and numbered them $k = 1, 2 \ldots$. We defined $\delta\varphi_k$ as the azimuthal angle between jet k and the $\not\!\!E_T$ vector; this is illustrated in Figure 5.5. In order to remove events with extremely poorly measured jets we rejected any event which had $\not\!\!E_T$ opposite ($\delta\varphi_k > (\pi - 0.1)$ for $k = 1, 2, 3$) or which had $\not\!\!E_T$ adjacent to ($\delta\varphi_k < 0.1$ for $k = 1, 2, 3$) any of the three leading jets. Furthermore, to reject those events in which fluctuations of the second jet masks the correlation with the first jet, we reject any event with $\sqrt{(\delta\varphi_1 - \pi)^2 + (\delta\varphi_2)^2} < 0.5$. Figure 5.6 is a scatter plot showing the correlation between $\delta\varphi_1$ and $\delta\varphi_2$ for a sample

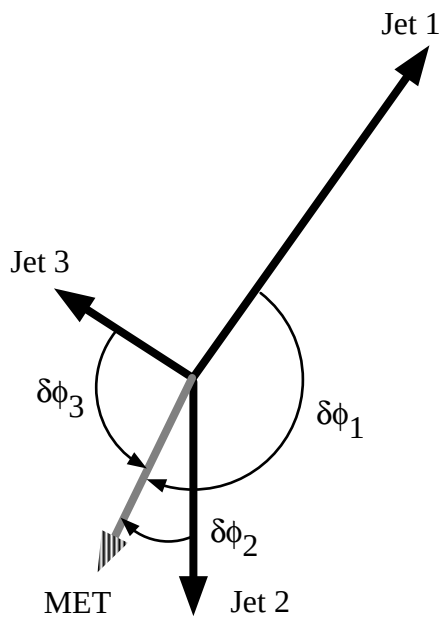

Figure 5.5: The definition of the angles $\delta\varphi_k$ used in the jet-$\not{E}_T$ correlation cut.

of events collected by the JET_MIN trigger, which required an $r = 0.7$ cone jet with $E_T > 20$ GeV; only events with $\not{E}_T > 20$ GeV and at least 'good' jets with $E_T > 15$ GeV are included in the plot. These data demonstrate the clustering of QCD events near the point $(\delta\varphi_1, \delta\varphi_2) = (\pi, 0)$ and the reason for the $\delta\varphi_1$–$\delta\varphi_2$ correlation cut. The cluster becomes stronger as the $\not{E}_T$ threshold is raised.

A total of 30 events passed this cut.

5.1.7 Electron and Muon Cuts

The decay $W \to \ell\bar{\nu}$ is a significant Standard Model source of real $\not{E}_T$. In order to remove these events we rejected any event containing an identified electron or muon. We applied loose quality criteria for the identification in order to attain as high an efficiency as possible.

The SQGL requirement of Section 3.3.2 and the jet cuts of Section 5.1.4 (especially the requirement that the three calorimeter clusters with the greatest E_T be hadronic) removed most of the $W \to e\bar{\nu}$ events from the sample. To reinforce these cuts we used the same covariance matrix technique mentioned in Section 3.3.2 and in references [26, 27] and rejected any event with an electromagnetic cluster having $E_T > 20$ GeV and $\chi^2 < 200$. Since this cut was applied to the electrons after the energy correction a few events which passed the SQGL filter's similar cut were rejected. The efficiency with which this cut identifies electrons (and thus rejects the event) is more than 97% [27].

The removal of $W \to \mu\bar{\nu}$ events was more difficult due to imperfect hit

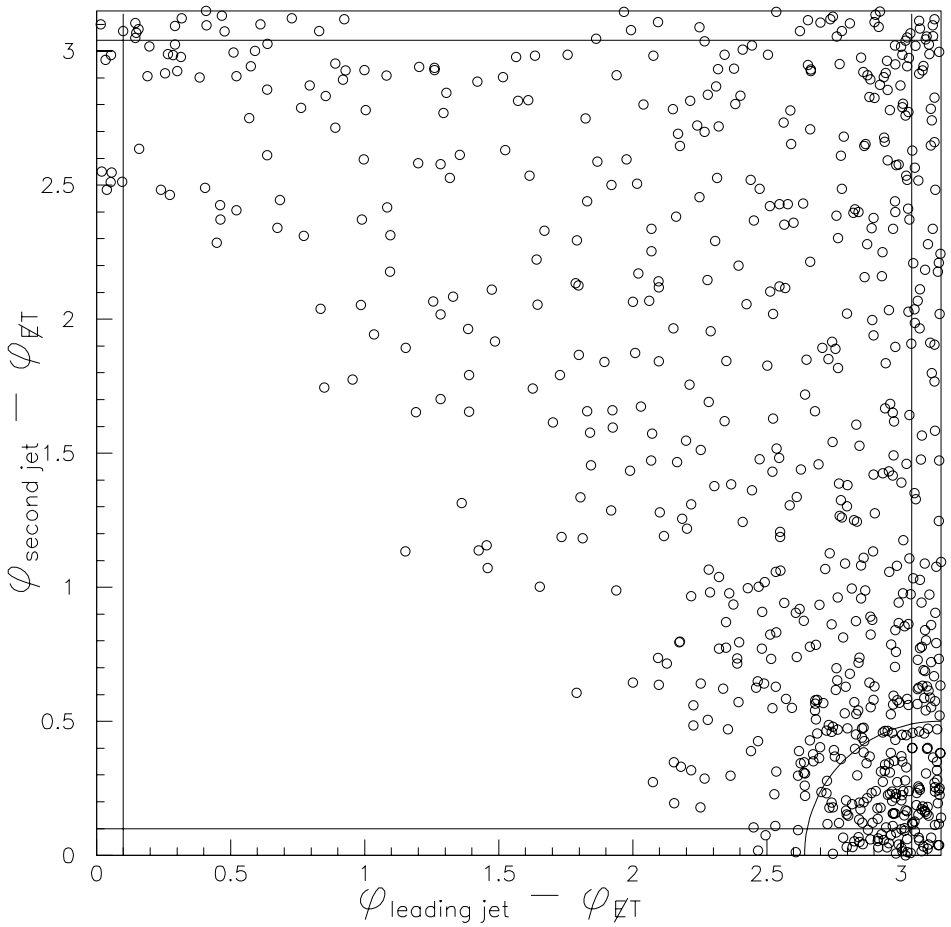

Figure 5.6: The correlation of $\delta\varphi_1$ and $\delta\varphi_2$ for events collected by a trigger requiring one jet with $E_T > 20$ GeV; only events with $\not{E}_T > 20$ GeV and three 'good' jets with $E_T > 15$ GeV are included. The lines indicate the boundaries of the regions removed by the cuts listed in section 5.1.6.

finding efficiency (70–85%), muon reconstruction efficiency (85%) and geometric acceptance (63–77%). We rejected any event containing a muon with $p_T > 15$ GeV if the muon satisfied the quality cuts IFW4 ≤ 1 and $\mathrm{ECAL}_\mu \geq 0.5$ GeV. IFW4 is an integer-valued quality flag which is zero for a 'perfect' muon track and is incremented by one for each failure of the following five loose track quality tests:

- a track was found in a module for each layer;
- distance of closest approach in z of the track to the interaction vertex, measured in the rz plane (the *nonbend view*) ≤ 100 cm;
- distance of closest approach of the track to the xy position of the beam measured in the $r\varphi$ plane (the *bend view*) ≤ 80 cm;
- nonbend view track fit has hit residual rms ≤ 7 cm;
- bend view track fit has hit residual rms ≤ 1 cm.

ECAL_μ is the sum of the energy seen in the cells which are intersected by the muon track and their nearest neighbors. Studies show the energy deposited by an energetic muon is typically in the range 1–3 GeV depending upon the thickness of the calorimeter seen by the track. The efficiency of our quality cuts for real muons which have been found by the reconstruction is near 100%; including all the efficiencies listed above gives the final efficiency of these cuts for identifying muons with $p_T > 15$ as $46 \pm 10\%$. This error is dominantly systematic [38, 39, 40].

The decay $W \rightarrow \tau\bar{\nu}$ was somewhat more difficult to reject; at the time of this analysis DØ did not have a mature tau identification algorithm. However, some fraction ($17.93 \pm 0.26\%$) of the taus decay to an electron (plus neutrinos), and others ($17.58 \pm 0.27\%$) decay to a muon (plus neutrinos); these were rejected by identification of the electron or muon. Since the hadronic decay of the tau leaves behind a tau neutrino the $\not\!\!E_T$ spectrum for these events is somewhat softer than $W \rightarrow e\bar{\nu}$; thus the 75 GeV $\not\!\!E_T$ cut was very effective in removing them.

A total of 25 events passed this cut.

5.1.8 Noise Cut

The jet quality requirements of Section 5.1.4 were applied only to the leading three jets in each event. Even after these cuts there remained some events containing a fourth (or higher number) jet which looked more like noise than a real jet. An additional cut against events containing any jet of $E_T >$ 15 GeV failing the 'good' jet requirement of Section 5.1.4 removed such cases.

A total of 17 events passed this cut.

5.1.9 Scanning

The 17 events passing the noise cut were scanned for anomalies.

We found one event which contained a 'muon' consistent with a cosmic ray. This muon was out-of-time with the collision by 150 ns, had good fit quality (IFW4 = 1) and was confirmed by an appropriate trace in the calorimeter

and a single central track match. It went through the region of the muon system near $\eta = 1.0$ where the magnetic field seen by a muon is small, so the momentum measurement was unreliable. Opposite the 'muon' track was a CDC track pointing to a calorimeter energy deposit which was dominantly electromagnetic. The longitudinal profile of this energy cluster was sufficiently unlike that of an electron or photon that the DØ electron finding algorithm did not even consider it a candidate. We rejected this event. Since the probability of a cosmic ray muon coincidence in a randomly chosen event is small, the efficiency for keeping signal events for this scanning was $\sim 100\%$.

We found two events in which the vertex finding algorithm failed to find the correct primary interaction vertex and found instead either a 'fake' vertex (the accidental coincidence of several tracks) or a minimum bias vertex distant from the hard scattering vertex. This behaviour was an unintended feature of the algorithm. When these event were re-reconstructed from the correct vertex each had a $\not{E}_T$ much less than 75 GeV. We rejected these two events. Scanning of a large number of events selected from the full data set showed that this vertex finding error is rare. In several hundred events scanned during data collection we observed no such error. It is the large $\not{E}_T$ requirement which enriched our sample in such events. Because the likelihood of a randomly selected event suffering such a vertex finding error was small, the efficiency of this scanning was $\sim 100\%$

Our final sample contained 14 events. Figure 5.7 is a histogram of the $\not{E}_T$ distribution for these events. The largest $\not{E}_T$ value of the sample is 168 GeV. Table 5.2 contains a summary of all our analysis cuts and the number

of events that pass each stage of the analysis.

Cut	Number of events passing
SQGL filter	9625
Single vertex and Scalar E_T	3811
Vertex z restriction	3730
$\not\!\!E_T > 75$ GeV	107
3 'good' jets with $E_T > 25$ GeV	47
Leading jet not in ICR	45
Reject Jet-$\not\!\!E_T$ correlation	30
Reject electrons and muons	25
Noise removal	17
Scanning	14

Table 5.2: A summary of the cuts used in this analysis and the number of events passing each cut.

5.2 Backgrounds

In any search for new physics one must understand what *known* physical processes mimic the signature of the new. For our analysis this meant we had to determine the number of events from Standard Model processes that can be expected to pass the cuts of Section 5.1. There are two important sources of background events in the Standard Model: the production and decay of vector bosons in association with jets and the production of multiple quark and gluon jets due to QCD. We discuss these backgrounds in the following sections.

There are two methods that may be used for determining the magnitude

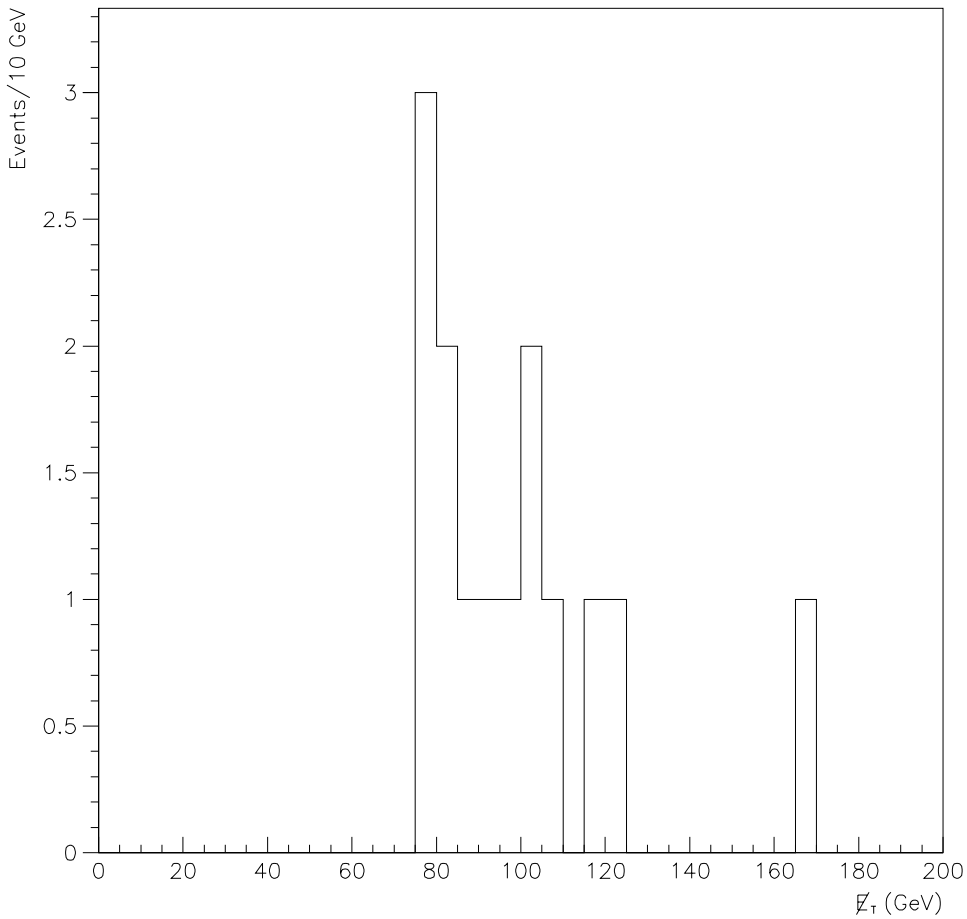

Figure 5.7: The $\not{E}_T$ distribution of the 14 events passing all our analysis cuts.

of the Standard Model backgrounds: data or Monte Carlo. When possible, we prefer to use the data; for the QCD background this was possible. The small number of W or Z plus multiple jet events available, and the unfinished status of the analysis of those samples, forced our reliance on Monte Carlo estimates of the vector boson backgrounds.

5.2.1 Vector Boson Associated Background

The processes $p\bar{p} \rightarrow W + n$ jets and $p\bar{p} \rightarrow Z + n$ jets with the subsequent decay $W \rightarrow \ell\bar{\nu}$ or $Z \rightarrow \nu\bar{\nu}$ both are copious sources of events with real $\not{E}_T$ carried away by one or more neutrinos. In addition decays of the W or Z to leptons may produce $\not{E}_T$ if the leptons are missed or are poorly measured and misidentified as we saw was the case for electrons in the ICR and is the case of undetected muons. The hadronic decays of the W and Z are inconsequential compared to the much larger cross section for QCD production of multiple jet events.

We used the Monte Carlo generator VECBOS [41] coupled with ISAJET [42] to produce both W and Z plus n jet events. VECBOS is a leading order parton level Monte Carlo generator which produces W and Z bosons in association with exactly n jets. The user specifies the value of n, which may be as large as four for W and three for Z production, and also the radius (in $\eta \times \varphi$) and minimum E_T of the jet. We used a radius of 0.5 to match that of our data analysis, and a minimum E_T of 10 GeV, to avoid any threshold effect from our 25 GeV jet requirement. We used ISAJET to 'dress' the partons. A slightly modified

ISAJET performed fragmentation and hadronization and could thus produce more than n jets from VECBOS's n jet event. VECBOS reports the cross section for the production of n *or more* jets, and for its proper use one must select the value of n appropriate for the analysis. Since we were interested in events with three or more jets, we produced Monte Carlo samples with three or more hadronic jets, counting hadronic decays of the tau lepton as hadronic jets. The cross sections calculated with VECBOS carry small statistical errors but significant systematic errors due to uncertainty in the value of α_s; we have assigned a 10% systematic error per jet for $n = 1 \ldots 3$.

To determine the response of the detector to these events we used the DØ detector simulation SHOWERLIBRARY [43]. SHOWERLIBRARY is based on DØGEANT, which is a detailed simulation of the DØ detector built with the general purpose detector simulation tool GEANT [44]. This Monte Carlo produces the same event format as the real data, allowing us to use the same software to analyze data and Monte Carlo. We used a detailed simulation of the DØ trigger system [45] to simulate the trigger hardware (L1) response to these events. We determined the trigger software (L2) response by applying the same L2 code as was used on the data to the Monte Carlo events.

The simulated events were reconstructed with the same version of the reconstruction program DØRECO as was used for our data. In Monte Carlo events the partons themselves are available for inspection; therefore energy corrections for reconstructed jets were much easier to develop than were the data corrections. In place of the jet corrections described in Section 4.2.1 we used a simpler correction derived by comparing reconstructed jet E_T to

partonic jet E_T, with the partonic jet defined with the same cone size as the calorimeter jet. The η and E_T dependent correction was tuned so that a sample of jets with partonic $p_T^{\rm part}$ had a mean corrected $E_T = p_T^{\rm part}$.

No detector simulation is perfect. To avoid known and suspected flaws, a few of the cuts listed in Section 5.1 were not used on the simulated events. Instead their effects were determined directly from the data. These cuts included the jet quality cuts and muon identification. It is not clear that the SHOWERLIBRARY Monte Carlo adequately reproduces the cell-by-cell details of the energy deposits within jets. Although the distribution of jet EM fraction produced by SHOWERLIBRARY is close to that observed in the data, no tuning has been done to reproduce the ratio of highest energy to second highest energy cell. Rather than rely on the simulation we applied the efficiency of the jet quality cuts as given in Section 5.1.4 for each of the three jets required in the event. In addition the muon reconstruction efficiency for DØRECO v10 is known to have been much greater for Monte Carlo than for data. For this reason we cut on the existence of a muon with the same $p_T > 15$ GeV at the Monte Carlo particle level. We applied the efficiency given in Section 5.1.7 for each muon.

Table 5.3 contains the results of the Monte Carlo background calculations. The table contains, for each background process, the cross section times branching fraction ($\sigma_{\rm VB} \cdot {\rm BF}$), the fraction ε_B of events passing all cuts, the *visible* cross section $\sigma_{\rm vis}$, which is the cross section predicted to pass our cuts, and finally the number $N_{\rm exp}$ of events expected in 7.4 pb^{-1} .

The cross section is determined with VECBOS; the branching fraction

includes both the branching fraction for the given decay of the W or Z and that of the tau lepton, where appropriate. The branching fractions and their errors are those given by the Particle Data Group [46]. The statistical errors reflect the small statistical error in the VECBOS cross section and the errors in the branching fractions from the Particle Data Group; the systematic errors include the 10% per jet systematic error in the cross section from VECBOS.

The statistical errors in ε_B were determined according to the binomial distribution and are significant because of the small absolute number of events passing the final selection cuts for each sample.[1] The errors due to the uncertainty of the jet efficiency and the muon efficiency are relatively small, and have been included in quadrature with the binomial error in the listed statistical errors. The systematic error is due to the uncertainty in the energy scale; $\pm 5\%$ is our best estimate of the systematic scale error between corrected data and corrected Monte Carlo. The influence of this scale error was determined by varying our final jet E_T and $\not{E}_T$ thresholds by $\pm 5\%$. The quoted systematic error reflects the difference in the number of Monte Carlo events passing the cuts when raised and lowered. An underestimate of the energy scale corresponds to cutting on higher energies than we realize, and thus produces lesser efficiencies; an overestimate has the opposite effect. ———————— table ——————————

We subjected the entire Monte Carlo sample to simulation of each of the

[1]Progress in this search would be greatly helped by much larger Monte Carlo event samples. It is impractical to do this with 'brute force'. This could be achieved either with a fast, rather than detailed, detector simulation or by judicious preselection of events at the generating stage, before detector simulation, or both.

Process	$N_{\rm jets}$	$\sigma_{\rm VB} \cdot {\rm BF}$ (pb)	ε_B (%)	$\sigma_{\rm vis}$ (pb)	$N_{\rm exp}$
$W \to e\bar{\nu}$	3	$54.2 \pm 4.7 \pm 16.2$	$0.62 \pm 0.14^{+0.03}_{-0.06}$	$0.34 \pm 0.08^{+0.10}_{-0.11}$	$2.47 \pm 0.60^{+0.75}_{-0.78}$
$W \to \mu\bar{\nu}$	3	$54.2 \pm 9.6 \pm 16.3$	$1.38 \pm 0.23^{+0.52}_{-0.28}$	$0.75 \pm 0.18^{+0.36}_{-0.27}$	$5.51 \pm 1.35^{+2.66}_{-1.99}$
$W \to \tau_h\bar{\nu}$	2	$116.5 \pm 17.7 \pm 23.3$	$0.27 \pm 0.07^{+0.15}_{-0.04}$	$0.32 \pm 0.10^{+0.18}_{-0.08}$	$2.34 \pm 0.72^{1.33}_{-0.56}$
$W \to \tau_\ell\bar{\nu}$	3	$19.4 \pm 3.0 \pm 5.8$	$1.39 \pm 0.27^{+0.34}_{-0.37}$	$0.27 \pm 0.07^{+0.10}_{-0.11}$	$1.99 \pm 0.50^{+0.77}_{-0.79}$
$Z \to e\bar{e}$	3	$4.96 \pm 0.05 \pm 1.5$	—	—	—
$Z \to \mu\bar{\mu}$	3	$4.95 \pm 0.07 \pm 1.5$	$1.41 \pm 0.31^{+0.26}_{-0.17}$	$0.070 \pm 0.016^{+0.025}_{-0.023}$	$0.51 \pm 0.11^{+0.18}_{-0.17}$
$Z \to \nu\bar{\nu}$	3	$30.0 \pm 0.6 \pm 9.0$	$2.26 \pm 0.33^{+0.49}_{-1.0}$	$0.68 \pm 0.10^{+0.25}_{-0.37}$	$4.98 \pm 0.74^{+1.85}_{-2.70}$
$Z \to \tau_h\bar{\tau}_h$	1	$22.5 \pm 0.3 \pm 2.3$	—	—	—
$Z \to \tau_h\bar{\tau}_\ell$	2	$7.6 \pm 0.19 \pm 1.5$	$0.49 \pm 0.10^{+0.11}_{-0.13}$	$0.037 \pm 0.008^{+0.011}_{-0.012}$	$0.27 \pm 0.06^{+0.08}_{-0.09}$
$Z \to \tau_\ell\bar{\tau}_\ell$	3	$0.62 \pm 0.03 \pm 0.19$	$1.00 \pm 0.26^{+0.21}_{-0.18}$	$0.006 \pm 0.002^{+0.002}_{-0.002}$	$0.05 \pm 0.01^{+0.02}_{-0.02}$

Table 5.3: Expected backgrounds from W and Z production in association with jets. The notation τ_ℓ indicates the process includes the leptonic decay of the τ; the notation τ_h indicates the hadronic decay of the τ.

eight different trigger configurations. We combined their results according to the ratios of the integrated luminosities collected under each trigger configuration. Our offline cuts were much stricter than the cuts used in the triggers; as expected, the triggers were all close to 100% efficient for events that passed the offline cuts. We observed no significant variations in efficiency between different trigger configurations for any of the Monte Carlo samples.

The visible cross section $\sigma_{\rm vis}$ listed in Table 5.3 is the product of the fraction of events passing the cuts and the process cross section calculated with VECBOS. The statistical errors were determined from the statistical errors in $\varepsilon_{\rm B}$ and $\sigma_{\rm VB}$; they are dominated by the statistical error in $\varepsilon_{\rm B}$. The systematic errors include the systematic errors in $\varepsilon_{\rm B}$ and $\sigma_{\rm VB}$ added in quadrature. Since the energy scale error is unrelated to the uncertainty in the value of α_s , the source of error in the VECBOS cross section, we believe it is reasonable to combine them.

The expected number of events is the visible cross section times the integrated luminosity used in this analysis. The statistical error reflects the statistical error in the visible cross section; the systematic error reflects the systematic error in the visible cross section combined with the systematic error in the luminosity, combined in quadrature. Since these systematic errors are unrelated, we believe it is reasonable to combine these errors.

Two of the background samples, $Z \rightarrow e\bar{e} + 3$ jet and $Z \rightarrow \tau_h\bar{\tau}_h + 1$ jet, each were counted as contributing zero events. For both of these backgrounds the full Monte Carlo sample was rejected early enough in the series of cuts that their contribution was clearly negligible. This was expected since neither of

these backgrounds produces real E_T; the $Z \rightarrow e\bar{e}$ events contain no neutrinos, and the $Z \rightarrow \tau_h \bar{\tau}_h$ contain relatively soft neutrinos that on average travel in opposite directions, and at least partly balance in p_T.

The sum of our predictions for all W and Z backgrounds is $18.1 \pm 1.9^{+7.6}_{-7.1}$ events. We have combined the statistical errors in quadrature but the systematic errors linearly, to reflect their correlated nature. The combined W and Z background cross section is $2.46 \pm 0.25^{+1.04}_{-0.97}$ pb.

5.2.2 QCD Associated Background

Unlike the W and Z associated backgrounds, we were able to determine the QCD associated background directly from the data. In fact, since the QCD background is due to large and therefore rare fluctuations we would not expect the detector simulation to represent it adequately, even if the number of simulated events which would be needed to obtain a significant sample of such large fluctuations were not prohibitively large.

The data sample used to determine the QCD associated background was collected by the JET_MIN trigger, which required one L1 trigger tower with $E_T > 3$ GeV and at L2 required one jet ($r = 0.7$ cone) with $E_T > 20$ GeV. Because the event rate from this trigger is so large, the trigger definition included a "prescale of 1000"; that is, only one in 1000 events which satisfied the jet requirement at L1 was passed on to L2. The total integrated luminosity represented by this sample was 7.8 ± 0.9 nb^{-1}. The events were corrected with the same algorithm used in the rest of the analysis.

The relatively low integrated luminosity of the JET_MIN sample is both a blessing and a curse. It guarantees that there shall be no significant contamination of the signal for which we seek, because the signal cross section is small. However, it also makes it necessary for us to fit and extrapolate the data in order to achieve a reasonable estimate on the number of events in our sample. Figure 5.8 shows the $\not\!\!E_T$ distribution for the JET_MIN trigger sample after one of our analysis cuts, specifically the jet-$\not\!\!E_T$ correlation cuts of Section 5.1.6; in this case we applied the cuts to up to three jets, since there was no previous requirement that there be three or more jets in the event. There is no event with $\not\!\!E_T > 75$ GeV. If we require the presence of three or more jets with $E_T > 25$ GeV, we find only five events with $\not\!\!E_T > 20$ GeV and none with $\not\!\!E_T > 30$ GeV. If one were merely to use Poisson statistics to set a 95% confidence level limit on the number of events passing the three jet and $\not\!\!E_T$ requirement, having seen zero events, this would then produce an expected background upper limit of less than three events in 7.4 nb^{-1} , which would translate to less than ≈ 3000 events in 7.4 pb^{-1} . This is clearly much stricter than a 95% confidence level limit; the 75 GeV $\not\!\!E_T$ threshold is far higher than any $\not\!\!E_T$ value seen in the sample. The naive application of Poisson statistics does not give a useful limit in this instance.

We chose instead to fit a phenomenological curve to the data. Since too few events passed the three jet requirement for us to use that cut before the $\not\!\!E_T$ cut, we determined the number of QCD events expected to pass both in two steps. The first step was to determine the $\not\!\!E_T$ spectrum before the three jet requirement, and the second was to determine what fraction of the events

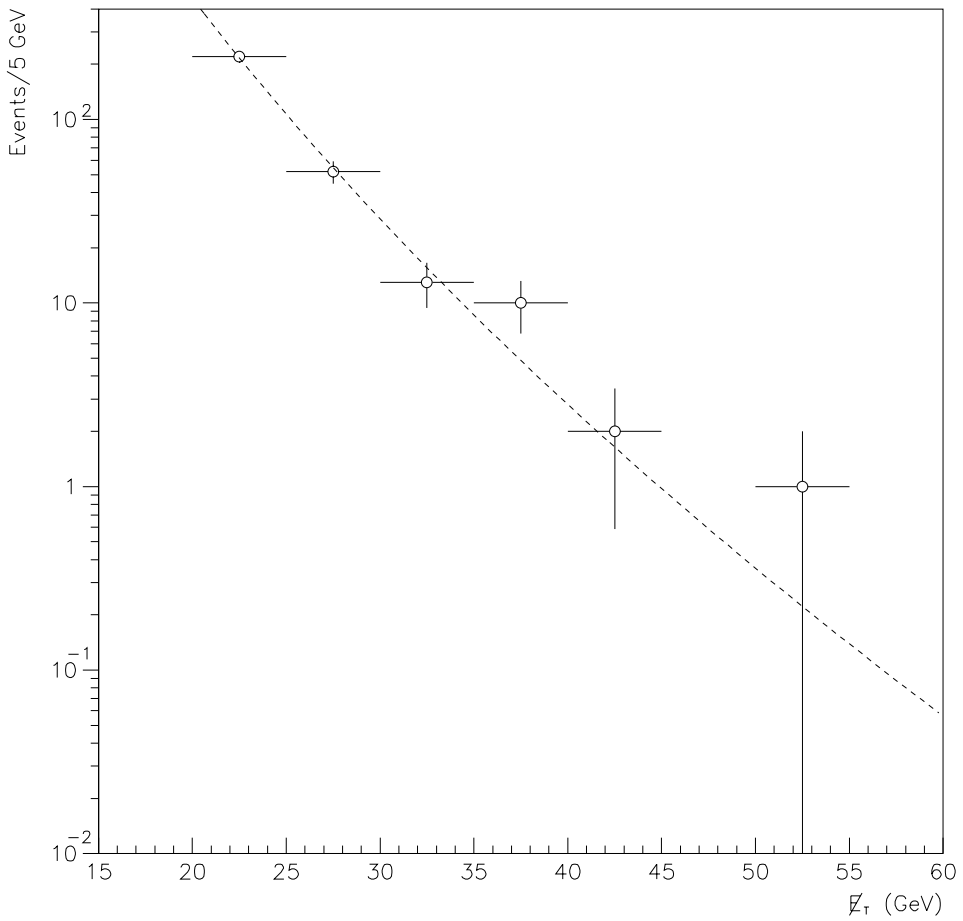

Figure 5.8: The $\not{E}_T$ distribution of the JET_MIN data sample, after imposition of jet-$\not{E}_T$ correlation cuts.

passing the $\not\!\!E_T$ cut would also pass the three jet requirement.

We found that the data of Figure 5.8 were fit well by a curve of the form $y(x) = \alpha e^{-\sqrt{\beta x}}$, where α and β are constants determined by minimizing the χ^2 of the fit. To make the extraction of the number of events with $\not\!\!E_T > 75$ GeV as simple as possible, we cast this distribution in the form

$$n(x) = \frac{N\beta e^{-(\sqrt{\beta x} - \sqrt{75\beta})}}{2(1 + \sqrt{75\beta})}. \tag{5.5}$$

In this form the fit parameters are N and β; β determines the rate of decrease of the curve and N is a normalization parameter defined such that the integral of the curve above $\not\!\!E_T = 75$ GeV is N. The fit to the data in Figure 5.8 gave $N = (29.8 \pm 22.6) \cdot 10^{-3}$ events in 7.8 nb^{-1} . When scaled up to a luminosity of 7.4 pb^{-1} the number of events is 28 ± 21 events expected with $\not\!\!E_T > 75$ GeV.

To determine the fraction of the events with $\not\!\!E_T > 75$ GeV which would pass the requirement of three or more jets with $E_T > 25$ GeV we divided the sample into bins in $\not\!\!E_T$, and determined the fraction of events passing the three jet requirement as a function of the $\not\!\!E_T$ of the sample. Table 5.4 contains the data used for this determination. Fitting a straight line to these fractions and extrapolating to $\not\!\!E_T = 75$ GeV gives $1.5 \pm 0.3\%$ as our prediction for the fraction of events passing. These data and the fit are shown in Figure 5.9. Combined with the result above for the number of events expected with $\not\!\!E_T > 75$, the final result is an expected 0.42 ± 0.37 events due to QCD.

Our need to extrapolate the fit of Figure 5.9 is unavoidable. Nevertheless, the projected number of background events is much smaller than the background expected from the vector bosons; even an estimate an order of

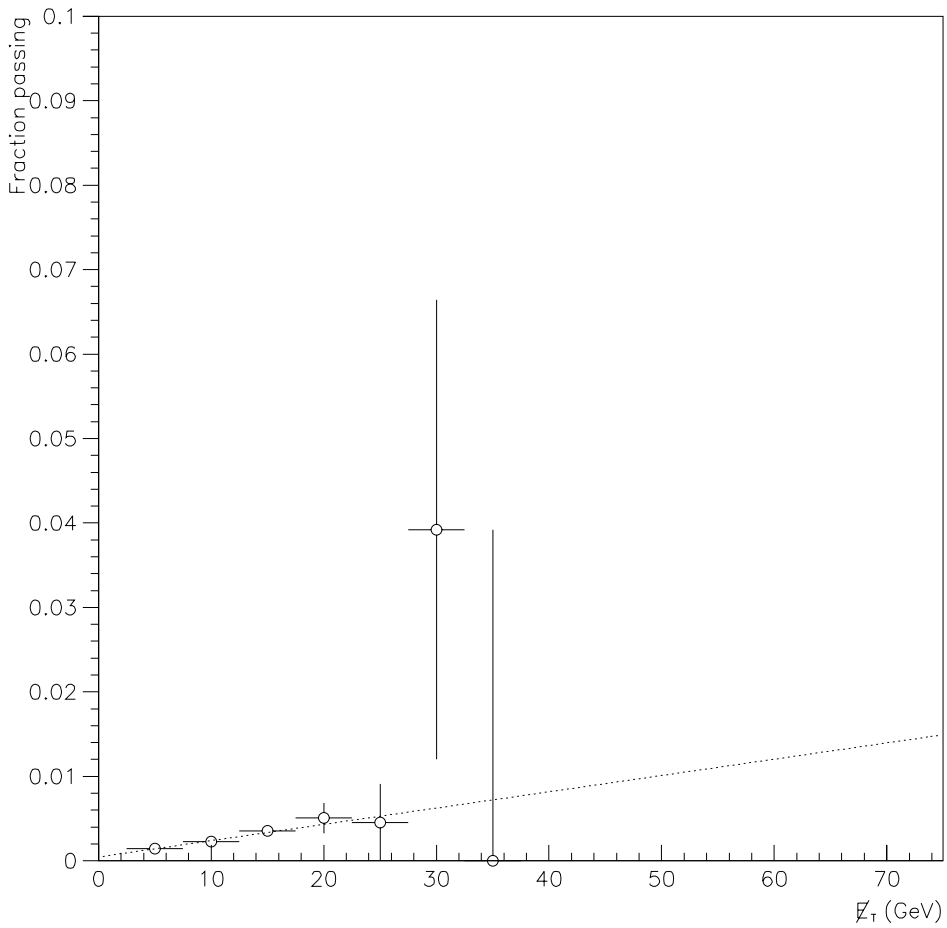

Figure 5.9: The fraction of events passing our three jet requirement as a function of the $\not{E}_T$ of the events.

$\not\!\!E_T$range (GeV)	$N_{\rm pass}$	$N_{\rm tot}$	Fraction passing (%)
0 – 5	88	60319	0.15 ± 0.02
5 – 10	122	53350	0.23 ± 0.02
10 – 15	41	11517	0.36 ± 0.06
15 – 20	8	1576	0.51 ± 0.18
20 – 25	1	220	0.46 ± 0.46
25 – 30	2	51	4.0 ± 2.7
30 – ∞	0	25	—

Table 5.4: The fraction of events satisfying the requirement of three or more jets with $E_T > 25$ GeV as a function of the $\not\!\!E_T$ of the events.

magnitude larger would yield a prediction small compared with the errors in the sum of the vector boson backgrounds. Furthermore, we see no excess events and have no indication that this estimate is in error.

The sum of the vector boson and QCD backgrounds is $18.5 \pm 1.9^{+7.6}_{-7.0}$ events, which is larger than and consistent with our observed number of events. We have no excess of events unexplained by the Standard Model.

Chapter 6

Results and Conclusion

Lacking any evidence for non-Standard Model production of events with large $\not{E}_T$ and multiple jets, the final step in our search is the simulation of the expected signal from squark and gluino production and decay and the extraction of cross section and mass limits from the data. In this chapter we describe the specific model used and the limits we extracted.

6.1 Specification of the Model

The Minimal Supersymmetric Standard Model (as described in Chapter 1) has too many free parameters to allow a fully exhaustive search. Reasonable progress is made by fixing all parameters except the gluino and squark masses. In choosing values for the fixed parameters we were guided by previous experimental searches and the limits they have set. The LEP experiments have essentially excluded squarks and charginos below the kinematic limit of 45 GeV and neutralinos below about 23 GeV [47]. In the MSSM these limits may

be transformed into a limit on the gluino mass; the limit depends on the values of μ and $\tan(\beta)$ chosen for the model. The chargino and neutralino limits are weakened by some choices of μ and $\tan(\beta)$. We have chosen values of these parameters which are consistent with existing LEP limits, and have chosen a large value of m_{H^+} as preferred by most theorists. The parameters we fixed were the following:

- $\mu = -250$ GeV.
- $\tan(\beta) = 2.0$,
- $m_{H^+} = 500$ GeV,

The branching fractions for each squark and gluino decay mode are slowly varying functions of these parameters.

To produce signal events we used the generator ISASUSY [48]. ISASUSY is an extension of the generator ISAJET which models the production of squarks and gluinos in $p\bar{p}$ collisions, and their subsequent decay according to the constraints of the MSSM. The version of ISASUSY we used included neither the production of scalar leptons (sleptons) nor scalar top quarks (stop squarks). The exclusion of sleptons is approximately equivalent to setting their mass to be the same magnitude as the squark mass. The exclusion of a separate stop squark means that we are sensitive to the other five squark flavors, but not to the production of the (lighter) stop, which has a different signature than the heavier squarks. Thus our analysis shall not set a limit on the mass of a light stop, but rather on the mass of the heavier squarks.

To calculate cross sections, we used the program SUSYXS, which includes the same code as ISASUSY for the calculation of cross sections but does not generate events. Our version of SUSYXS uses the EHLQ structure function [49]. Since the cross section calculations have been done only to leading order, and since for the production of heavy objects it is the structure function values for large momentum fractions which matter, the choice of structure function parameterization has little impact. What has greater impact for the cross section calculation is the choice of the scale at which α_s is calculated and the factorization scale used for the structure function. SUSYXS uses the same scale for both. Changing the scale from $4\hat{s}$ to $\hat{s}/4$ produces approximately a factor of two change in the production cross section. We have chosen to take a middle value of $\hat{s}$ as the scale for our calculations, and have studied how changing the scale from $4\hat{s}$ to $\hat{s}/4$ alters our results.

6.2 Signal Efficiencies

We generated events for 28 different combinations of $m_{\tilde{q}}$ and $m_{\tilde{g}}$. Each of the samples was analyzed in the same manner as the simulated backgrounds described in Chapter 5. Table 6.1 contains the results of the signal calculations. The table contains, for each signal sample, the gluino and squark masses ($m_{\tilde{g}}$ and $m_{\tilde{q}}$), the total production cross section $\sigma_{\rm tot}$, and our detection efficiency $\tilde{\varepsilon}$. The cross section was calculated with SUSYXS using the structure functions and q^2 scale given above. The statistical and systematic errors in $\tilde{\varepsilon}$ were determined in the same manner as described for the background samples.

$m_{\tilde{g}}$	$m_{\tilde{q}}$	$\sigma_{\rm tot}$ (pb)	$\tilde{\varepsilon}$ (%)	$m_{\tilde{g}}$	$m_{\tilde{q}}$	$\sigma_{\rm tot}$ (pb)	$\tilde{\varepsilon}$ (%)
100	100	1420	$4.62 \pm 0.68^{+1.39}_{-0.96}$	220	220	7.45	$19.75 \pm 2.04^{+1.37}_{-0.69}$
100	150	630	$1.76 \pm 0.40^{+0.50}_{-0.60}$	221	200	11.7	$18.07 \pm 1.94^{+1.37}_{-0.94}$
100	500	435	$1.20 \pm 0.33^{+0.13}_{-0.26}$	225	300	1.77	$17.17 \pm 1.55^{+1.55}_{-1.55}$
150	100	472	$4.91 \pm 0.70^{+1.25}_{-0.82}$	225	500	1.35	$15.24 \pm 1.76^{+1.55}_{-1.21}$
150	200	50.4	$7.63 \pm 0.91^{+0.89}_{-1.08}$	250	250	2.60	$25.35 \pm 2.38^{+1.03}_{-1.47}$
150	300	28.1	$7.62 \pm 0.92^{+1.10}_{-1.08}$	250	50	4990	$0.26 \pm 0.10^{+0.10}_{-0.00}$
150	400	28.4	$6.30 \pm 0.81^{+1.36}_{-0.74}$	275	275	1.11	$26.97 \pm 2.12^{+1.55}_{-0.65}$
150	500	30.6	$7.54 \pm 1.19^{+1.30}_{-1.39}$	300	150	27.8	$11.67 \pm 1.19^{+1.72}_{-0.86}$
175	300	9.48	$11.56 \pm 1.51^{+1.91}_{-2.17}$	300	200	6.18	$20.06 \pm 2.06^{+1.03}_{-2.14}$
175	500	10.0	$10.31 \pm 1.42^{+1.56}_{-1.56}$	400	100	159	$3.43 \pm 0.78^{+0.86}_{-1.20}$
200	150	53.4	$15.41 \pm 1.43^{+1.55}_{-2.09}$	400	150	21.1	$8.30 \pm 1.25^{+1.93}_{-2.03}$
200	200	15.6	$18.56 \pm 1.62^{+0.77}_{-1.45}$	400	200	4.41	$17.08 \pm 1.53^{+2.00}_{-1.54}$
200	220	10.4	$19.04 \pm 2.01^{+0.51}_{-1.80}$	400	250	1.08	$25.26 \pm 2.02^{+2.06}_{-1.49}$
200	400	3.12	$14.37 \pm 1.37^{+1.38}_{-1.86}$	500	100	143	$1.44 \pm 0.36^{+0.34}_{-0.34}$

Table 6.1: Squark and gluino production cross sections and detection efficiencies for our 28 simulated event samples.

It was impractical to generate event samples on a fine enough mass grid to allow easy determination of our signal detection efficiency for every point in the ($m_{\tilde{g}}$, $m_{\tilde{q}}$) plane. Instead, we used a combination of linear fitting and linear interpolation. We selected four sets of samples:

- all with $m_{\tilde{g}} = 400$ GeV;
- all with $m_{\tilde{q}} = 300$ GeV;
- all with $m_{\tilde{q}} = 500$ GeV;

- all with $m_{\tilde{g}} = m_{\tilde{q}}$;

and fit a straight line to each set to determine the variation of efficiency with squark mass (along the $m_{\tilde{g}} = 400$ GeV line) or gluino mass (along the $m_{\tilde{q}} = 300$ GeV and $m_{\tilde{q}} = 500$ GeV lines) or both (along the $m_{\tilde{g}} = m_{\tilde{q}}$ line). Figure 6.1 contains plots of these efficiencies and the linear fits to the plots. In all cases the quality of the fit was good. The error bars on the points show the statistical errors only; the dotted lines show the systematic errors, determined by repeating the fits for systematically high and low efficiencies as given in Table 6.1.

To determine our efficiency at a point $(m_{\tilde{g}}, m_{\tilde{q}})$ we used linear interpolation between the appropriate bounds from Figure 6.1. We propagated statistical errors with the standard technique, including the effect of the correlation between the slopes and intercepts of the linear fits. We propagated systematic errors by linear interpolation between the high and low systematic fits.

6.3 Cross Section Limits

To determine our cross section limit we first must determine the signal cross section $\tilde{\sigma}$ to which we are sensitive. This is the cross section observed minus the cross section predicted for the backgrounds scaled by our signal efficiency,

$$\tilde{\sigma} = \frac{\Big((N - n_{\mathrm{QCD}})/\mathcal{L}\Big) - \sigma_{\mathrm{vis}}}{\tilde{\varepsilon}}. \tag{6.1}$$

where $N = 14$ is the number of events seen in the data, $n_{\mathrm{QCD}} = 0.42 \pm 0.37$ is our predicted number of events from QCD, $\sigma_{\mathrm{vis}} = 2.46 \pm 0.25^{+1.04}_{-0.97}$ is our

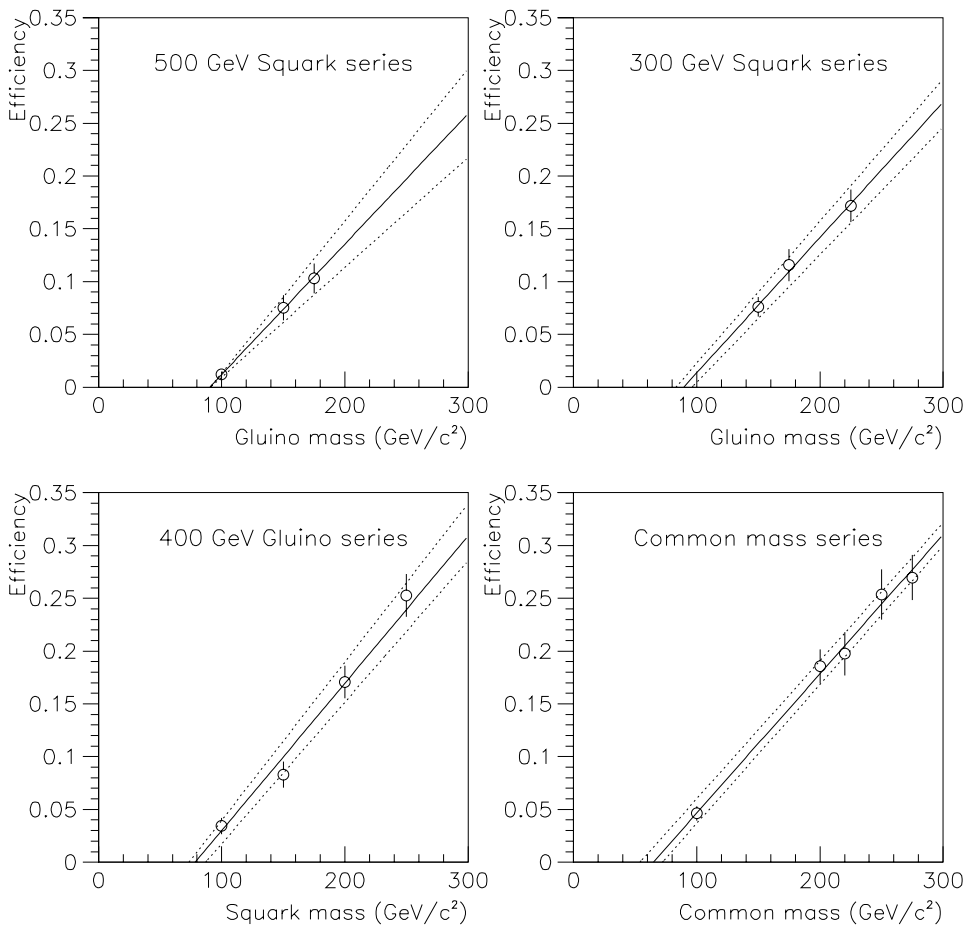

Figure 6.1: The signal efficiencies for selected $(m_{\tilde{g}}, m_{\tilde{q}})$ and the fits used in interpolating between them. The error bars are statistical only. The solid lines are the fits to the nominal efficiencies and the dotted lines show the systematic errors. The values of the fit χ^2 per degree of freedom are, from upper left to lower right, 0.031, 0.20, 1.27, and 0.20.

predicted W and Z background cross section, and $\tilde{\varepsilon}$ is our signal efficiency, which varies with $m_{\tilde{g}}$ and $m_{\tilde{q}}$.

The calculation of the upper limit to any confidence level α from this formula is in theory quite simple. Assuming one knows the (properly normalized) distribution P of $\tilde{\sigma}$, one merely determines what value $\tilde{\sigma}_\alpha$ satisfies the requirement that the probability content of the interval $[0, \tilde{\sigma}_\alpha]$ equals α:

$$\alpha = \int_0^{\tilde{\sigma}_\alpha} P(\sigma)\, d\sigma. \tag{6.2}$$

The difficultly, of course, is in the details. One frequently does not know the distribution governing errors; Gaussian errors are usually assumed. In our case the number of events seen is sufficiently large (14) that we use the Gaussian distribution with width $\sqrt{14}$ rather than the exact Poisson distribution to describe it; we assume all other statistical errors are Gaussian. The Gaussian distribution is not, however, appropriate for the systematic errors.

The decision of how to handle systematic errors in the setting of a limit is sometimes a difficult one. There exists an established theory for the handling of statistical errors, but not for systematic errors, which are *not* statistical. Indeed it is most often the case that one cannot determine an accurate probability content for a systematic error estimate, and that it reflects instead the "reasonable" variation of some parameter, fit method, or choice of model. Some authors, while recognizing that systematic errors are not statistical, decide to handle them in as if they were. We have done this to some extent in our combination of systematic errors leading up to the errors in $\sigma_{\rm vis}$ and $\tilde{\epsilon}$, although we have taken care that the errors we have combined come from

unrelated sources. For our final limit calculation, we prefer to handle the systematic errors in a conservative fashion. For each $(m_{\tilde{g}}, m_{\tilde{q}})$ we compute $\tilde{\sigma}$ four times, allowing each of $\sigma_{\rm vis}$, $\mathcal{L}$ and $\tilde{\varepsilon}$ to vary from its nominal value to it nominal plus and minus one systematic error interval. The energy scale uncertainty influences both $\sigma_{\rm vis}$ and $\tilde{\varepsilon}$; in each calculation we take the error in the same direction for both. We then choose the largest of the calculated values, $\tilde{\sigma}'$, as the conservative central value to be used in the limit calculation, and use the statistical error $\delta\tilde{\sigma}$ as the width of the Gaussian distribution. For the 95% confidence level limit $\tilde{\sigma}_{95\%}$ we solve the equation

$$0.95 = \frac{\int_0^{\tilde{\sigma}_{95\%}} d\sigma \, e^{-\left((\sigma-\tilde{\sigma}')/\delta\tilde{\sigma}\right)^2/2}}{\int_0^{\infty} d\sigma \, e^{-\left((\sigma-\tilde{\sigma}')/\delta\tilde{\sigma}\right)^2/2}} \tag{6.3}$$

for $\tilde{\sigma}_{95\%}$. Since $\tilde{\varepsilon}$ is a function of $m_{\tilde{q}}$ and $m_{\tilde{g}}$ this cross section limit also depends on them. Table 6.2 gives our 95% confidence level cross section limit for various $m_{\tilde{g}}$ and $m_{\tilde{q}}$.

6.4 Mass Limits

To turn our cross section limit into a gluino and squark mass limit we use the calculation of the production cross section obtained with SUSYXS. We merely compare, point by point, our cross section limit with the calculated cross section; if our limit is lower than the calculated cross section, then the point is excluded at the 95% confidence level. As discussed above there is substantial uncertainty (due to the different α_s and factorization scale choices) in the cross section calculation. Figure 6.2 shows the region excluded by our

	$m_{\tilde{g}}$ (GeV)						
$m_{\tilde{q}}(GeV)$	100	150	200	250	300	350	400
100	38.0	41.6	44.9	49.0	53.9	60.2	68.5
150	47.5	14.8	15.2	15.6	16.1	16.6	17.1
200	64.4	16.6	9.2	9.4	9.5	9.7	9.9
250	102.9	19.0	10.4	6.7	6.8	6.9	6.99
300	256.4	22.3	11.9	8.1	5.2	5.3	5.4
350	225.1	22.5	12.1	8.3	6.3	4.3	4.4
400	222.2	22.8	12.3	8.4	6.4	4.6	3.7

Table 6.2: Our 95% confidence level cross section limit (in picobarns) for the production of gluinos and squarks in $p\bar{p}$ collisions at a center of mass energy of 1.8 TeV, as a function of $m_{\tilde{g}}$ and $m_{\tilde{q}}$.

search at the 95% confidence level and the band of uncertainty induced by the cross section error. Henceforth we shall refer to the middle contour as our limit; the reader should keep in mind the approximately ± 10 GeV effect of the cross section uncertainty. The reader should also note that our analysis did not explore the low mass regions (below 100 GeV) except for the one point $m_{\tilde{g}} = 250$ GeV, $m_{\tilde{q}} = 50$ GeV, since most of this region had been excluded by previous experiment.

In the limit of $m_{\tilde{q}} \gg m_{\tilde{g}}$, gluino pair production dominates over the other two processes, and the gluino decay patterns are insensitive to further increase in the squark mass. In this region we produce an asymptotic limit of $m_{\tilde{g}} > 157$ GeV at the 95% confidence level. In the case of equal squark and gluino masses, we produce a limit $m_{\tilde{g}} = m_{\tilde{q}} > 218$ at the 95% confidence level. In the limit of heavy gluinos the model eventually breaks down. Recall that

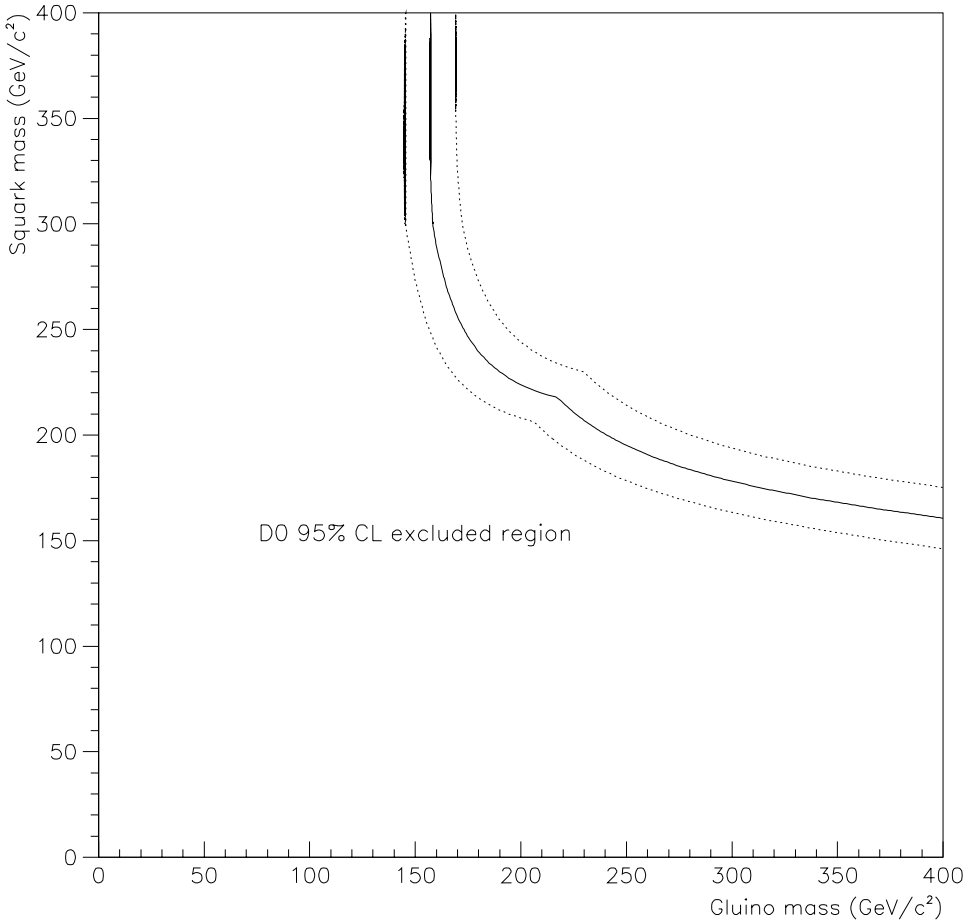

Figure 6.2: The DØ 95% confidence level exclusion contour. The solid line is the result of using an α_s and factorization scale of $\hat{s}$; the upper dotted line is for $\hat{s}/4$ and the lower is for $4\hat{s}$.

the mass of $\tilde{Z}_1$, the LSP, depends on the $m_{\tilde{g}}$. Thus the gluino cannot become too much heavier than the squark, or the squark would become the LSP; the existence of a charged, color-bearing stable squark would have long ago been detected. Before that extreme is reached, the $\tilde{Z}_1$ becomes sufficiently massive that the $\not{E}_T$ signal from the decay $\tilde{q} \rightarrow q\tilde{Z}_1$ becomes small, and our signal detection efficiency becomes negligible. Thus for sufficiently heavy gluinos we can set no limit on the squark mass. We have not yet produced any simulated events in this region of the ($m_{\tilde{g}}$, $m_{\tilde{q}}$) plane, and can state only that the gluino mass for which we can set no squark mass limit is above 400 GeV. Although we are confident that our efficiency interpolation is accurate in the regions between our existing simulated signal samples, we do not want to extrapolate the fits beyond the region we have investigated. Evaluation of the sample at $m_{\tilde{g}} = 250$ GeV and $m_{\tilde{q}} = 50$ GeV does allow us to exclude that point at the 95% confidence level; using Equation 6.3 we obtain a 95% confidence level upper limit on the cross section of 340 pb, while the MSSM cross section is in the range 3900–6600 pb, depending on the scale choice. Similarly, the point at $m_{\tilde{g}} = 500$ GeV and $m_{\tilde{q}} = 100$ GeV is excluded; our cross section limit is 57 pb, while the MSSM cross section is in the range 106–193 pb.

6.5 Comparison with Previous Results

Our search was not extended to low squark and gluino masses, since they have already been excluded by previous work. The LEP experiments provide a lower mass limit of 45 GeV for the squark and a gluino mass limit that

depends on the choices of $\tan(\beta)$ and μ. CDF provides a gluino mass limit of 30 GeV $\leq m_{\tilde{g}} \leq$ 95 GeV in the limit of heavy squarks for the same choices of $\tan(\beta)$ and μ used in our analysis [50]. Earlier results from UA1 and UA2 did not employ the MSSM, but excluded the ranges 4 GeV $\leq m_{\tilde{g}} \leq$ 53 GeV and 16 GeV $\leq m_{\tilde{g}} \leq$ 79 GeV; in the lower mass regions the assumption that the gluino decays via $\tilde{g} \rightarrow q\bar{q}\tilde{\gamma}$ is not far different from the prediction of the MSSM [51, 52]. Searches for the decays $\psi \rightarrow \gamma\eta_{\tilde{g}}$ and $\Upsilon \rightarrow \gamma\eta_{\tilde{g}}$, where $\eta_{\tilde{g}}$ is the pseudoscalar $\tilde{g}\tilde{g}$ bound state, exclude $m_{\tilde{g}} \leq$ 1 GeV and $m_{\tilde{g}} \leq$ 3 GeV, respectively [53]. The possible existence of a "light gluino window" around 3 GeV is still a matter of dissent. The CDF squark mass limit of reference [50] depends on the mass of gluino, as does our own. CDF sets no squark mass limit when $m_{\tilde{g}}$ is greater than 410 GeV. We have refrained from extending our exclusion contour into the region above $m_{\tilde{g}} = 400$ GeV because at this time we lack sufficient simulated signal samples in that region; however, the single sample we have at $m_{\tilde{g}} = 500$ GeV, $m_{\tilde{q}} = 100$ GeV demonstrates that we can extend existing limits in that region as well. These results are all summarized in Figure 6.3.

6.6 Future Considerations

In the present Tevatron run (Run IB) we expect to collect up to 75 pb^{-1} of integrated luminosity; this will help to extend our search to heavier masses. More important, however, are some improvements of technique.

DØ should soon publish measured cross sections for the process $p\bar{p} \rightarrow$

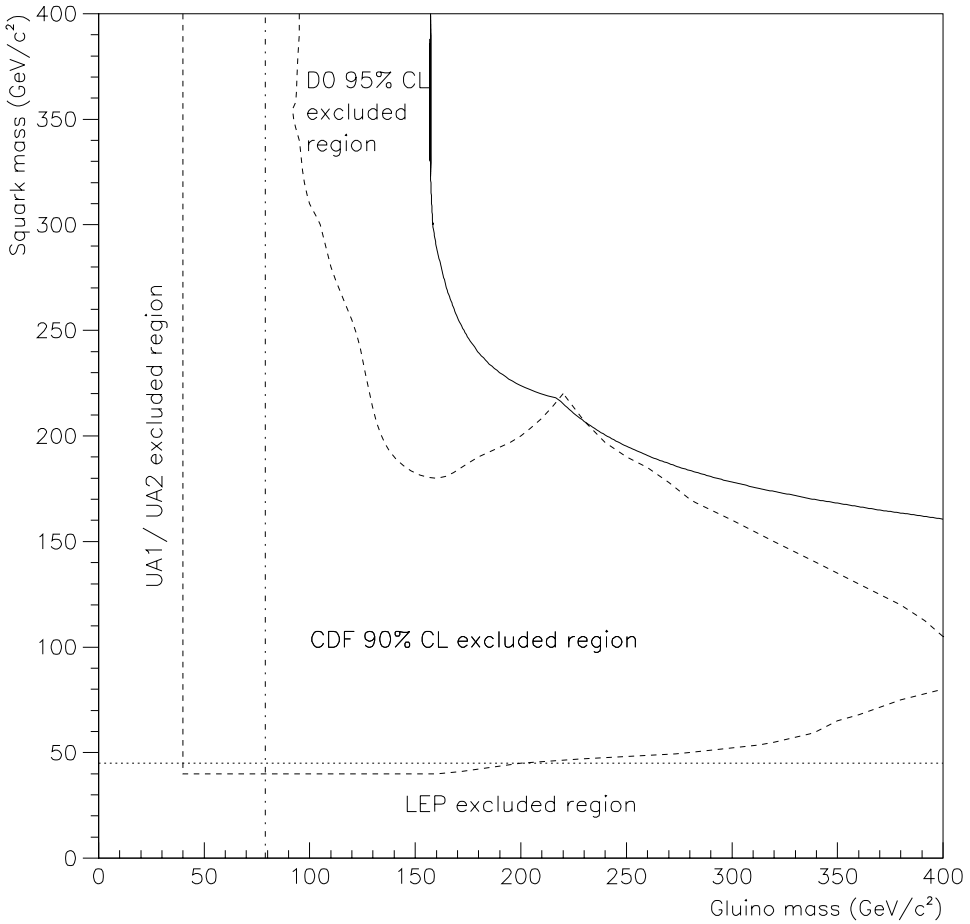

Figure 6.3: Current squark and gluino mass limits. Left of the dot-dashed line is the gluino mass region excluded by UA1 and UA2. Below the dotted line is the squark mass region excluded by the LEP experiments. Inside the dashed line is the CDF 90% confidence level excluded region. Below the solid line is the DØ 95% confidence level excluded region.

$W + n$ jets. Once the analysis on these data is mature, we should be able to avoid the large systematic uncertainties of the Monte Carlo determination of W and Z backgrounds; we may modify the $W \rightarrow e\bar{\nu}$ events by removing the electron to make an event like $Z \rightarrow \nu\bar{\nu}$, or replace the e by a μ or simulated τ.

An increase in both the number and size of simulated signal samples would make interpolation of efficiency easier and reduce the statistical error in the efficiency calculations. To obtain the number and size of samples necessary a new and faster detector simulation, specifically tuned to reproduce DØ's jet and $\not{E}_T$ response, is needed. Extension of our search to heavier masses also requires, of course, producing additional simulated samples at those masses.

The greatest sensitivity to new physics from the MSSM will come from combining results from all the supersymmetry searches underway in the collaboration; searches for charginos and neutralinos, scalar top, and multilepton decays of squarks and gluinos are all underway. And finally, one can hope to see a signal at last, and be faced with the happy problem of determining the masses of the superparticles and testing the theory in more detail.

Bibliography

[1] T.D. Lee, **Symmetries, Asymmetries, and the World of Particles**, p. 57, University of Washington Press (1988).

[2] S. Weinberg, Phys. Rev. Lett **19**, 1264 (1967).

[3] G. Arnison *et al.*, Phys. Lett. **122B**, 103 (1982).

[4] G. Arnison *et al.*, Phys. Lett. **126B**, 398 (1983).

[5] M. Banner *et al.*, Phys. Lett. **122B**, 476 (1983).

[6] P. Bagnaia *et al.*, Phys. Lett. **129B**, 130 (1983).

[7] G. Ross, **Grand Unified Theories**, Benajamin/Cummings (1984).

[8] Y. Golfand and E. Likhtman, JETP Lett. **13**, 323 (1971).

[9] D. Volkov and V. Akulov, Phys. Lett. **46B**, 109 (1973).

[10] J. Wess and B. Zumino, Nucl. Phys. **B70**, 39 (1974).

[11] X. Tata, in **The Standard Model and Beyond**, p. 304, ed. J. Kim, World Scientific, Singapore (1991); H. Nilles, Phys. Rep. **110**, 1 (1984);

P. Nath, R. Arnowitt, and A. Chamseddine, **Applied N=1 Supergravity** (ICTP Series in Theoretical Physics, Vol. 1), World Scientific, Singapore (1984); H. Haber and G. Kane, Phys. Rep. **117**, 75 (1985).

[12] H. Baer, M. Drees, and X. Tata, Phys. Rev. **D41**, 3414 (1990).

[13] H. Baer *et al.*, Phys. Lett. **161B**, 175 (1985).

[14] H. Baer, V. Barger, D. Karatas, and X. Tata, Phys. Rev. **D36**, 96 (1987).

[15] H. Baer, X. Tata, and J. Woodside, Phys. Rev. **D41**, 906 (1990).

[16] U.Amaldi *et al.*, Phys. Lett. B 281 (1992).

[17] W. Thompson, State University of New York at Stony Brook, Ph. D. Thesis, *Search for the Top Quark in the Muon + Jets Channel at D0* (1994) (unpublished).

[18] S. Abachi *et al.*, Nucl. Inst. and Meth., **A338**, (1993).

[19] D. Perkins, **Introduction to High Energy Physics, 2nd Edition**, Benjamin/Cummings (1982).

[20] M. Abolins *et al.*, Nucl. Instr. and Methods, **A280**, 36 (1989).

[21] S. Abachi *et al.*, Nucl. Instr. and Methods, bf A324, 53 (1993).

[22] J. Linnemann, in "Proceedings of the American Physical Society Division of Particles and Fields Conference", Fermilab (Nov. 1992), ed. R. Raja and J. Yoh.

[23] M. Abolins *et al.*, IEEE Trans. Nuc. Sci. **36**, No. 1 (1989).

[24] M. Fortner *et al.*, IEEE Trans. Nuc. Sci. **38** (1991).

[25] M. Paterno, DØ Internal Note 1782 (1993) (unpublished).

[26] R. Engelmann *et al.*, Nucl. Instr. and Methods **216**, 45 (1983).

[27] M. Narain, in "Proceedings of the American Physical Society Division of Particles and Fields Conference", Fermilab (Nov. 1992), ed. R. Raja and J. Yoh.

[28] U. Heintz and M. Narain, DØ Internal Note 1814 (1993) (unpublished).

[29] N. Hadley, DØ Internal Note 904 (1989) (unpublished).

[30] M. Paterno, DØ Internal Note 1374 (1992) (unpublished).

[31] The CDF Collaboration, F. Abe *et al.*, Phys. Rev. Lett. **69**, 2896 (1992).

[32] J. Bantly and Q. Li-Demarteau, DØ Internal Note 1691 (1993) (unpublished).

[33] J. Bantly, DØ Internal Note 1849 (1993) (unpublished).

[34] N. Amos, J. Linnemann, R. Partridge and L. Paterno, DØ Internal Note 2031 (1994) (unpublished).

[35] R. Astur, private communication.

[36] V. D. Elvira, J. Blazey, and R. Astur, DØ Internal Note 1763 (1993) (unpublished).

[37] M. Bhattacharjee, private communication.

[38] C. Gerber, P. Quintas, and D. Wood, DØ Internal Note 1718 (1993) (unpublished).

[39] C. Gerber, P. Quintas, and D. Wood, DØ Internal Note 1904 (1993) (unpublished).

[40] C. Gerber, private communication.

[41] F. Berends, W. Geile, H. Kuijf, and B. Tausk, FERMILAB-Pub-90/213-T (1990).

[42] F. Paige and S. Protopopescu, Brookhaven National Laboratory Report BNL-37066 (1985) (unpublished).

[43] W. Dharmaratna, R. Raja, and C. Stewart, DØ Internal Note 1730 (1993) (unpublished).

[44] R. Brun and F. Carminati, "GEANT Detector Description and Simulation Tool," CERN, CERN Program Library Long Writeup W5013 (1993).

[45] "D0$LEVEL1:L1SIM.DOC," DØ Online documentation.

[46] Phys. Rev. **D45**, "Review of Particle Properties".

[47] T. Medcalf, "The Search for Supersymmetry with the Aleph Detector at LEP"; P. Lutz, "SUSY with DELPHI"; B. Zhou, "Results of Supersymmetric Particle Searches with the L3 Detector"; R. Brown, "Searches for

New Particles in OPAL"; all in **International Workshop on Supersymmetry and Unification of Fundamental Interactions**, P. Nath ed., World Scientific, Singapore (1993).

[48] ISASUSY was written by H. Baer and X. Tata, and is an extension of ISAJET by F. Paige and S. Protopopescu. The physics included in ISASUSY was incorported into ISAJET in ISAJET 7.0.

[49] K. Ellis *et al.*, FERMILAB-Pub-86/75-T (1986).

[50] F. Abe *et al.*, Phys. Rev. Lett. **69** (1992).

[51] C. Albajar *et al.*, Phys. Lett **B198** (1987).

[52] J. Alitti *et al.*, Phys. Lett. **B235** (1990).

[53] J. Lee-Franzini, in "Supernova 1987A, One Year Later: Results and Perspectives in Particle Physics", in **Proceedings of Les Rencontres de Physique de la Valee d'Aosta**, M. Greco, ed., Editions Frontieres, Gif-sur-Yvette, France (1988).